nature physics

Article

https://doi.org/10.1038/s41567-025-02827-7

Single-fluorogen imaging reveals distinct environmental and structural features of biomolecular condensates

Received: 3 April 2023

Accepted: 12 February 2025

Published online: 14 March 2025

Check for updates

Tingting Wu[1,2,4], Matthew R. King[2,3,4], Yuanxin Qiu[1,2], Mina Farag[2,3], Rohit V. Pappu[2,3] ✉ & Matthew D. Lew[1,2] ✉

Biomolecular condensates are viscoelastic materials. Simulations predict that condensates formed by intrinsically disordered proteins are network fluids defined by spatially inhomogeneous organization of the underlying molecules. Here, we test these predictions and find that molecules within condensates are organized into slow-moving nanoscale clusters and fast-moving dispersed molecules. These results, obtained using single-fluorogen tracking and super-resolution imaging of different disordered protein-based condensates, affirm the predicted spatially inhomogeneous organization of molecules within condensates. We map the internal environments and interfaces of condensates using fluorogens that localize differently to the interiors versus interface between dilute phase and condensate. We show that nanoscale clusters within condensates are more hydrophobic than regions outside the clusters, and regions within condensates that lie outside clusters are more hydrophobic than coexisting dilute phases. Our findings provide a structural and dynamical basis for the viscoelasticity of condensates.

Biomolecular condensates provide spatial and temporal control over cellular matter and biochemical reactions[1]. Proteins with intrinsically disordered regions (IDRs), such as prion-like low-complexity domains (PLCDs) and arginine-glycine-rich (RG-rich) regions are prominent drivers of different types of condensates[2,3]. Several investigations have suggested that condensates are viscoelastic materials[4–10]. Despite the central importance of nano- and mesoscale organization of molecules to condensate viscoelasticity, these details have remained uncharacterized, even for simple one-component condensates.

Recent computations predicted that condensates formed by PLCDs and model telechelic polymers are defined by spatially inhomogeneous networks of the underlying molecules[11–13] (Fig. 1a). Internal networks in condensates are predicted to have dynamic hub-and-spoke organization, with hubs being nanoscale clusters of molecules that are generated by reversible physical crosslinks among molecules[11,12]. Here, we report results from experimental tests of computational predictions using single-molecule tracking and single-molecule orientation-localization microscopy (SMOLM). In these experiments, we combine freely diffusing fluorogenic probes[14–16] with single-molecule imaging[17–22] to characterize the spatial inhomogeneities, microenvironments, and dynamics of molecules within condensates.

Environmentally sensitive dyes change their fluorescence intensity (making them fluorogens) or colour (making them solvatochromic) based on their environment and their interactions[14–16,23–26] (Extended Data Fig. 1). We deployed fluorogenic molecules that are solvatochromic and used them as structural probes in super-resolution, single-molecule imaging to investigate condensates formed by human protein IDRs, including three variants of the PLCD of heterogeneous

[1]Department of Electrical and Systems Engineering, James F. McKelvey School of Engineering, Washington University in St. Louis, St. Louis, MO, USA. [2]Center for Biomolecular Condensates, James F. McKelvey School of Engineering, Washington University in St. Louis, St. Louis, MO, USA. [3]Department of Biomedical Engineering, James F. McKelvey School of Engineering, Washington University in St. Louis, St. Louis, MO, USA. [4]These authors contributed equally: Tingting Wu, Matthew R. King. ✉e-mail: pappu@wustl.edu; mdlew@wustl.edu

https://doi.org/10.1038/s41567-025-02827-7

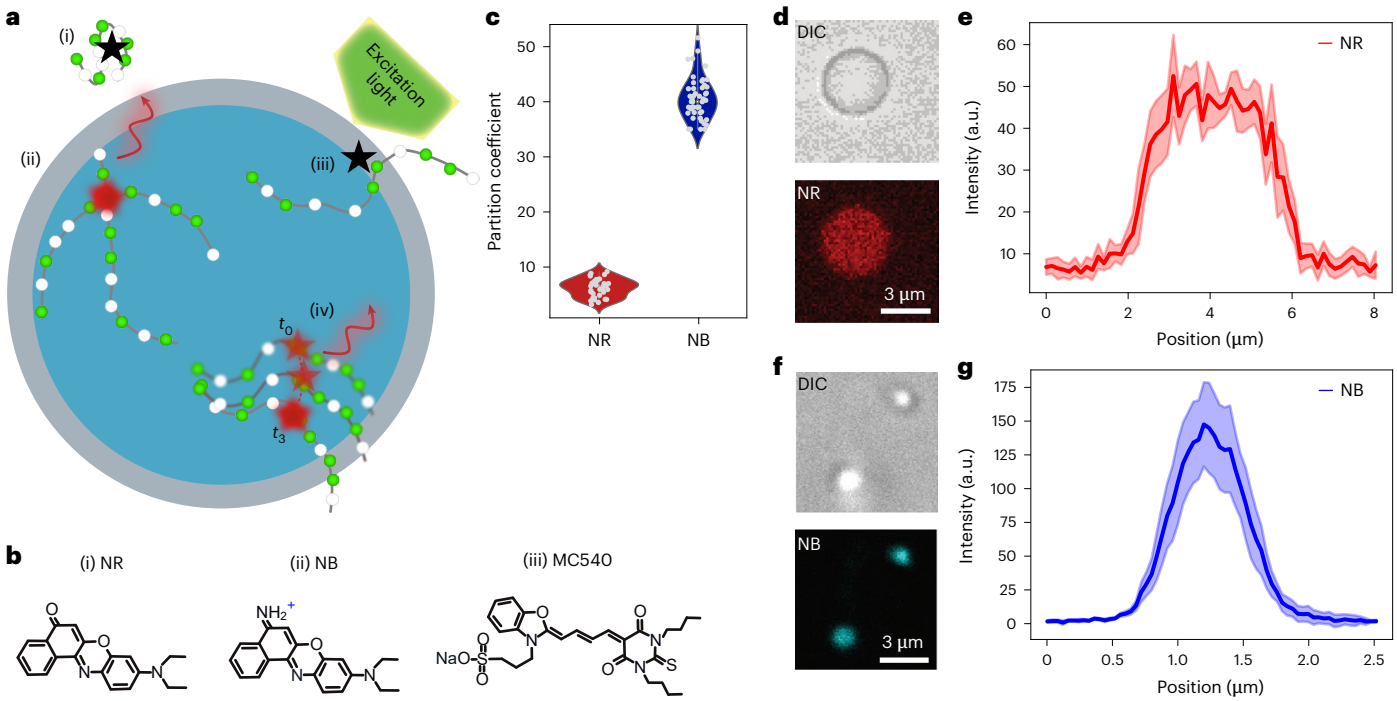

Fig. 1 | Partitioning of fluorogenic probes into biomolecular condensates. **a**, A1-LCD molecules, characterized by aromatic stickers (green) and non-aromatic spacers (white), form a network-like organization within condensates. As fluorogens (shown as black stars) diffuse through solution, they encounter different chemical environments in the dilute phase (white space outside), in the condensate (blue circle) and at the interface between the dilute phase and condensate (grey region). In response, they either remain dark ((i) and (iii)) (black stars) or become fluorescent ((ii) and (iv)) (red stars and curved arrows). Their ((ii), (iv)) speeds of movement and brightness are also affected. **b**, Chemical structures of the three different fluorogens used for imaging condensates: (i) NR, (ii) NB and (iii) MC540. **c**, Partition coefficients for NR and NB, measured for 37 condensates for NR for NB (grey circles) across two biological replicates. The median values are 6.5 and 40 for NR and NB, respectively. Shaded regions denote the probability density. **d**, Top, condensates formed by unlabelled A1-LCD molecules were imaged using differential interference contrast (DIC) microscopy. Bottom, NR partitions into A1-LCD condensates, and this fluorogen was imaged using point-scanning confocal microscopy (signal shown in the red channel). **e**, Line scan quantifications of partition coefficients of NR into A1-LCD condensates. **f**, Top, DIC images of A1-LCD condensates; bottom, confocal images showing the partitioning of NB into these condensates. **g**, Line scan quantifications of the partition coefficients of NB into A1-LCD condensates. For line scans **e** and **g**, five condensates across two biological replicates were used to derive median values (bold line) and the 95% confidence interval (shaded region).

nuclear ribonucleoprotein A1 (A1-LCD)[2,27] and the RG-rich IDR from DEAD-box helicase 4 (DDX4)[3,28]. Our measurements test the structural basis for measured viscoelastic properties[6,9,29,30] and predictions that have emerged from physical theory and computations[11–13,31].

The solvent quality, electrochemical properties, and hydrophobicity of condensate interiors are likely to be distinct from coexisting dilute phases[28,32–37]. We used different polarity-sensing fluorogens: Nile blue (NB), Nile red (NR)[14,15] and merocyanine 540 (MC540)[16]. These fluorogens are dark in aqueous solutions, even when they are pumped with an excitation laser. As the fluorogens diffuse through solution, they can either partition into hydrophobic environments or bind specifically to hydrophobic pockets within or outside condensates. This binding causes an increase in their fluorescence quantum yield and a shift in their absorption and emission spectra (Fig. 1a). We used the three fluorogens in separate measurements to probe the interiors and interfaces of condensates.

NR (Fig. 1b(i)) is minimally soluble in aqueous buffers, and it has a solubility of 280 µM (0.09 mg ml^{-1}) in a 1:10 mixture of dimethyl sulfoxide (DMSO) and phosphate buffered saline (PBS). By contrast, NB (Fig. 1b(ii)), which is essentially the same as NR, albeit with an amine, has a solubility in water of 0.14 M (50 g l^{-1}). The fluorogens, present at low micromolar or submicromolar concentrations in single-molecule measurements[38], freely diffuse in solution and through the condensates formed by untagged proteins. MC540 (Fig. 1b(iii)) partitions to interfaces between membranes and aqueous environments[16], so we used it as a probe of condensate interfaces.

We used point-scanning confocal microscopy to measure the partitioning of NR and NB into condensates formed by wild-type A1-LCD (Fig. 1c–g). The partitioning measurements were performed using 34 µM NR and 40 µM NB. Across ~50 distinct measurements, we obtained median values of 6.5 and 40 for the partition coefficients of NR and NB into A1-LCD-rich phases. The partition coefficient of NB is eight times higher than that of NR. In the single-molecule measurements, we used concentrations of 3.4 µM for NR and 2 nM for NB, which translates to dense phase concentrations of 17 µM and 0.08 µM for NR and NB, respectively. Ligands that stabilize dense phases will lower the macromolecular saturation concentration (c_{sat}), whereas ligands that destabilize dense phases will have the opposite effect[39,40]. We measured the effects of fluorogens on the c_{sat} values of A1-LCD molecules. These measurements were performed at two different temperatures and different bulk concentrations of each of the dyes. The data show that the dyes have negligible effects on the c_{sat} (Extended Data Fig. 2a,b). Overall, the solvatochromic fluorogens are non-perturbative when used at concentrations relevant for single-molecule imaging. Importantly, the controls establish that the features we extract from single-molecule measurements are direct consequences of interactions of the dyes with the macromolecules and not due to interactions of the dyes with themselves.

Fluorogens reveal spatial inhomogeneities within condensates

We leveraged the diffusion and transient binding of NB and NR[38,41] as a photo-switching ('blinking') mechanism for super-resolution,

https://doi.org/10.1038/s41567-025-02827-7

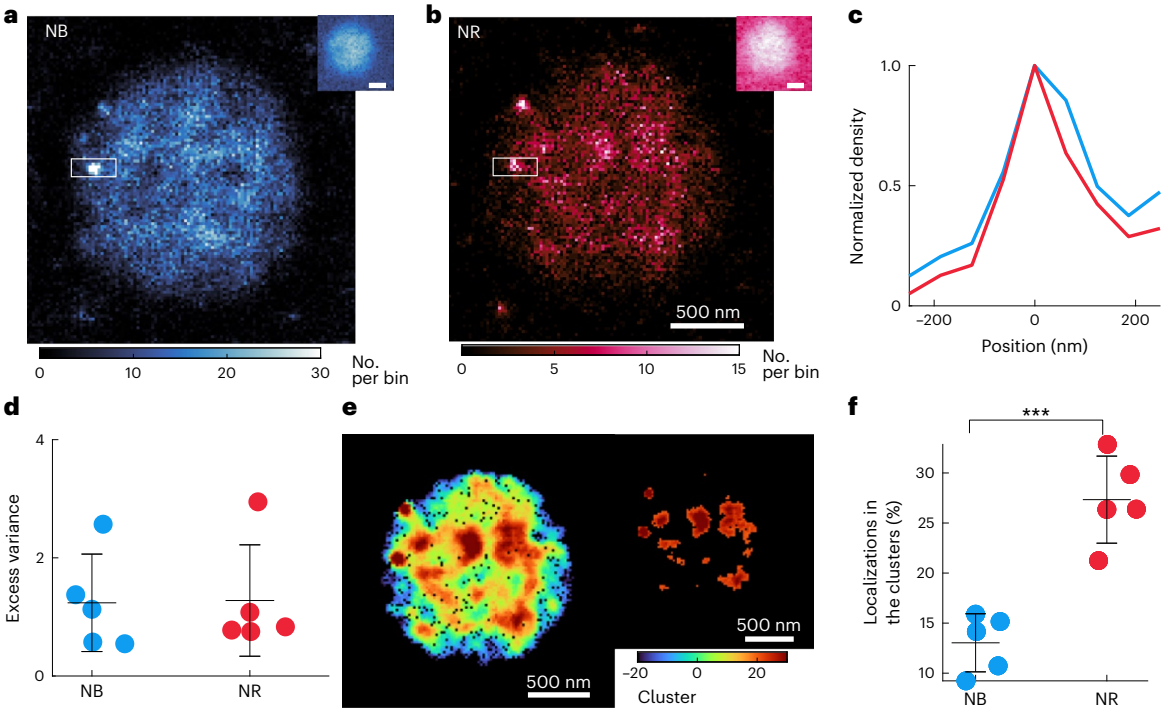

Fig. 2 | NB and NR bind to nanoscale clusters within condensates. a,**b**, SMLM images of a single A1-LCD condensate collected using NB (**a**) and NR (**b**). Insets, epifluorescence images. Scale bar 5 µm. Colour bars, number of single-molecule localizations within each 10-nm × 20-nm bin (white box). **c**, Localization line profile along the long axis of the white boxes in **a** and **b**. **d**, Quantifying the binding and activation of NB (blue) and NR (red) within five condensates using excess variance. Larger excess variance values represent greater heterogeneities in the blinking statistics of fluorogenic probes within a condensate; zero excess variance represents uniform blinking statistics throughout the condensate. **e**, A1-LCD condensate in **b** imaged by NR and colour-coded by clustering coefficient; molecules with clustering coefficients above a threshold of 20 are classified as being clustered. Inset, map of regions that contain clustered NR localizations. **f**, Percentages of single-molecule localizations that are spatially clustered for five condensates ($P = 4.9 \times 10^{-4}$). For excess variance and localization clustering calculations (**d** and **f**), five condensates across two biological replicates were used to derive mean (centre line) ± s.d. (error bars). $^{***}P < 10^{-3}$. All P values were calculated using Welch's unequal variances t-test (two-sided).

single-molecule localization microscopy (SMLM)[42–45]. As individual probes diffuse through solution, they remain dark until they encounter hydrophobic environments or bind to specific sites. If they are sufficiently immobilized within the pocket (for example, ~10 ms—the timescale of the camera integration time), then enough fluorescence signal can be accumulated to detect and localize single fluorogens. The fluorogens become dark when they leave the preferred sites[17]. Accumulating the positions of many blinking events yielded detailed SMLM maps of internal structures within condensates with nanoscale resolution and single-molecule sensitivity (Supplementary Video 1).

Super-resolution images of single condensates showed that both NR and NB exhibit non-uniform localization patterns (Fig. 2a,b). We measured digital on/off blinking of the fluorogens within apparent hotspots. These are repeated bursts of single-molecule fluorescence turning on and off via binding and unbinding/photobleaching. Based on computations[11], we refer to the hotpots as hubs that are formed by physically crosslinked macromolecules within condensates. We observed nanoscale hubs in SMLM images collected using both NR and NB (Fig. 2c); these data recapitulate inhomogeneities observed via epifluorescence imaging (Extended Data Fig. 3) but with superior spatial resolution and single-molecule sensitivity.

To quantify the spatial inhomogeneity using single-molecule blinking (Fig. 2d), we calculated the excess variance of the number of single-fluorogen localizations within a spatial pixel within each condensate (Methods). If a fluorogenic probe has a uniform probability of blinking across the entire condensate, then its localization density would be Poisson-distributed[46]. This would yield an excess variance of zero (Supplementary Fig. 3). The condensates imaged sequentially by NB and NR showed larger than expected variances with a mean excess variance of 1.3 ± 0.8 (s.d. 2.1×10^4 localizations per condensate on average). Thus, SMLM shows that both NB and NR exhibit large and significant spatial variations in their blinking dynamics (Fig. 2d).

The super-resolution images of NR reveal the presence of nanoscale hubs (Fig. 2c). We measured the relative proportion of localizations that are spatially clustered to quantify the relative affinities of NR and NB for the nanoscale hubs (Fig. 2e,f). For each localization, we compared the local and surrounding density and then computed a clustering coefficient[47,48]. Molecules with clustering coefficients above a threshold of 20 are classified as being clustered (Fig. 2e and Methods). For the five condensates imaged by NR and NB, 27 ± 3% of NR molecules and 13 ± 4% of NB molecules were clustered (Fig. 2f). This indicates that clustering was detected twice as often with NR when compared to NB. The implication is that although both probes exhibit a strong affinity to hubs, NR localized more strongly to hubs than NB.

Next, we quantified the similarities and differences between spatial inhomogeneities mapped using NR versus NB[49,50]. For images collected using both NR and NB, we found that the diffuse regions, characterized by small relative single-fluorogen localization densities, were mostly uncorrelated. However, regions exhibiting high NR and NB blinking events were highly correlated with one another (Extended Data Fig. 4). These data suggest that even though the affinities and binding lifetimes of the fluorogens at hubs are dye-specific, the presence of hubs and their identities, as measured by NR versus NB, were equivalent.

Slow-moving hubs coexist with fast-moving molecules

Our data indicate that nanoscale hubs are clusters of proteins that must be distinct local environments. Single-molecule imaging also shows

https://doi.org/10.1038/s41567-025-02827-7

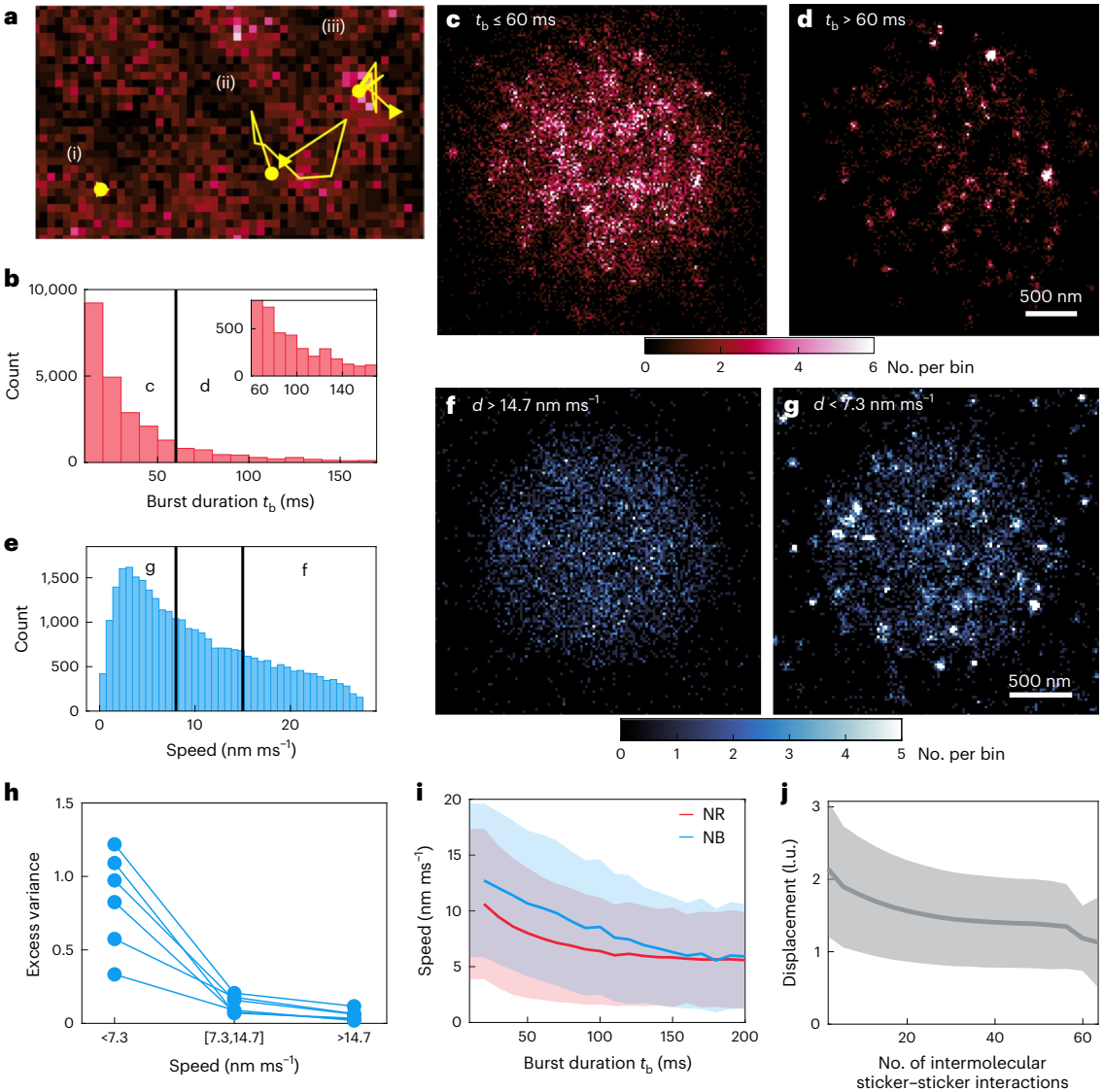

Fig. 3 | Single-fluorogen tracking uncovers inhomogeneous molecular organization and dynamics. a, Trajectories (yellow lines) connecting single NR localizations (yellow dots) exhibit both short (i) and long ((ii) and (iii)) burst durations, as well as high (ii) and low (iii) speeds. **b**, Burst duration t_b of each NR trajectory. The inset shows a zoom into the tail of the burst duration distribution. **c**,**d**, SMLM images of NR molecules with burst durations shorter than 60 ms (**c**) and longer than 60 ms (**d**) (partition shown as black line in **b**). Extended Data Fig. 5j,k shows burst duration data for NB. **e**, Speed distribution of NB measured between consecutive camera frames (10-ms exposure time). **f**,**g**, SMLM images of NB molecules with speeds larger than 14.7 nm ms^{-1} (**f**) and smaller than 7.3 nm ms^{-1} (**g**) (partitions shown as black lines in **e**). Extended Data Fig. 5e–g shows speed data for NR. **h**, Excess variance of NB localizations grouped by speeds (left, <7.3 nm ms^{-1}; middle, between 7.3 and 14.7 nm ms^{-1}; right, >14.7 nm ms^{-1}). Blue lines, excess variance of NB within each condensate. **i**, Speeds of NB (blue) and NR (red) as a function of their fluorescence burst durations. Lines, mean value averaged over 1.5×10^5 trajectories for NB and 129,000 trajectories for NR; shaded region, ±1 s.d. Six condensates were imaged across two biological replicates. **j**, Displacement in lattice units (l.u.) of each chain within a simulated A1-LCD condensate as a function of the number of intermolecular sticker–sticker interactions. Mean (line) ± s.d. (shaded region) shown. Results are from lattice-based Monte Carlo simulations[11] (three independent simulations per condensate type).

that nanoscale hubs within each of the condensates disappear from one location and reappear at nearby locations (Supplementary Videos 2 and 3). We probed these dynamics by tracking the movements and fluorescence burst durations of individual fluorogens (Supplementary Video 4). The burst duration t_b is correlated with the amount of time a fluorogen spends in a fluorescence-promoting environment. The speed measures the distance covered by a fluorogen within 10-ms intervals (Fig. 3a and Extended Data Fig. 5). As a fluorogen explores a condensate, changes in the local environment cause both its burst duration and its speed of movement to vary. The burst durations of NR range from 10 ms to more than 170 ms (Fig. 3b). This heterogeneity is highlighted by reconstructing SMLM images using only single molecules with short burst durations ($t_b \leq 60$ ms; Fig. 3c) versus those with long burst durations ($t_b > 60$ ms; Fig. 3d). Single molecules with short burst durations are distributed uniformly across the condensate, whereas hotspots are dominant in the long-burst-duration images. This trend was also observed when the condensates were imaged using NB (Extended Data Fig. 5i–k). However, when compared to NR, NB exhibits larger displacements (Extended Data Fig. 5b,d). These data are consistent with the observation that the NB dyes localize to equivalent hubs within condensates but their dwell times at the hubs are different from those of NR.

We separated NB emitters into three categories based on their speeds (10 ms exposure times; Fig. 3e). An SMLM image, reconstructed from high-speed emitters, shows a uniformly distributed localization density across the condensate (Fig. 3f). These fluorogens were localized

https://doi.org/10.1038/s41567-025-02827-7

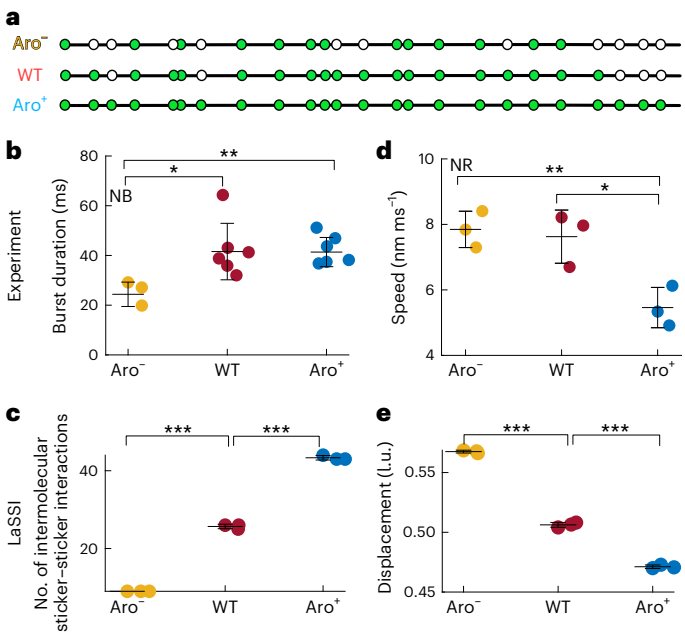

Fig. 4 | Nanoscale dynamics within condensates are influenced by the numbers of aromatic residues. a, Schematic showing the positions of aromatic amino acids as green circles in Aro$^-$, A1-LCD (wild type, WT) and Aro$^+$ variants. White circles denote non-aromatic spacers that are replaced by aromatic residues in Aro$^+$. Black lines represent all non-aromatic residues. **b**, Fluorescence burst durations for the three condensates measured using NB. $P_{Aro^-,WT} = 0.016$, $P_{Aro^-,Aro^+} = 0.0063$. Extended Data Fig. 6a(ii) shows burst duration data for NR. **c**, Number of intermolecular sticker–sticker interactions in simulated condensates. The sequence-specific simulations were performed using the LaSSI engine. $P_{Aro^-,WT} = 4.0 \times 10^{-4}$, $P_{WT,Aro^+} = 3.0 \times 10^{-6}$. **d**, Speed of NR within condensates formed by Aro$^-$, WT and Aro$^+$. $P_{Aro^-,Aro^+} = 0.0078$, $P_{WT,Aro^+} = 0.024$. Extended Data Fig. 6b(iv) shows speed data for NB. **e**, Displacements of protein chains quantified in simulated condensates. Circles in **b** represent the average burst durations of individual condensates; in **d**,**e** they represent the median values of measurement parameters for individual condensates. $P_{Aro^-,WT} = 1.3 \times 10^{-5}$, $P_{WT,Aro^+} = 3.6 \times 10^{-5}$. For NB imaging, three Aro$^-$ (30,300 ± 11,800 (mean ± s.d.) localizations each), six WT (60,400 ± 22,600 localizations each) and six Aro$^+$ (106,000 ± 53,200 localizations each) condensates across two biological replicates were used to derive mean (centre lines) ± s.d. (error bars). For NR imaging, three Aro$^-$ (12,100 ± 3,140 localizations each), three WT (40,400 ± 12,300 localizations each) and three Aro$^+$ (49,300 ± 19,500 localizations each) condensates (technical replicates). $^*P < 0.05$, $^{**}P < 0.01$, $^{***}P < 10^{-3}$. All P values were calculated using Welch's unequal variances t-test (two-sided).

within sufficiently hydrophobic environments to emit fluorescence but bind relatively weakly, resulting in relatively high speeds. An SMLM image reconstructed solely from low-speed emitters exhibits clusters and non-uniform localization patterns (Fig. 3g). This phenomenon is consistent across six different A1-LCD condensates, where the average excess variance of single-molecule images, reconstructed using emitters with low, medium and high speeds, are 0.84 ± 0.33, 0.13 ± 0.06 and 0.05 ± 0.04, respectively (Fig. 3h). Condensates imaged using NR showed similar trends (Extended Data Fig. 5e–g). Overall, NR and NB emitters with longer burst durations tend to have lower speeds (Fig. 3i). The hubs revealed by longer-burst emitters and those sensed by slowly moving emitters are consistent with one another (Fig. 3 and Extended Data Fig. 5).

We hypothesized that the nanoscale hubs uncovered using NR and NB are direct readouts of networked A1-LCD molecules formed via reversible, intermolecular physical crosslinks among aromatic residues, referred to as stickers[2,11,27]. To test this hypothesis, we probed the correlation between molecular displacements and the extent of crosslinking in simulated condensates (Methods). These simulations show that A1-LCD molecules that are part of densely crosslinked networks have smaller overall displacements (Fig. 3j). The nanoscale hubs observed using single-fluorogen imaging appear to be clusters of A1-LCD molecules defined by higher extents of reversible, physical crosslinking. The fluorogens become trapped for longer times in nanoscale hubs because of the higher local density of stickers within the clusters that underlie the hubs. We conclude that dynamical inhomogeneities (Fig. 3) are a consequence of spatial inhomogeneities (Fig. 2). Similar observations of dynamical inhomogeneities arising from spatial inhomogeneities have been reported by Shen et al.[51] using adaptive single-molecule tracking in condensates that form at the post-synaptic density. Likewise, computations that reproduce structure factors from small-angle neutron scattering measurements also show spatial and dynamical inhomogeneities[52].

Number of aromatic residues impacts dynamics of PLCDs

The driving forces for phase separation of A1-LCD and designed variants thereof are governed by the number and types of aromatic residues[2,27]. We used NR and NB dyes to obtain comparative assessments of nanoscale structures within condensates formed by two variants of the A1-LCD system designated as Aro$^+$ and Aro$^-$ (ref. 27). The Aro$^+$ variant has more aromatic residues dispersed uniformly along the linear sequence when compared to the wild-type A1-LCD, whereas Aro$^-$ has fewer aromatic groups[27] (Fig. 4a and Supplementary Table 1).

When probed using NB, the condensates formed by Aro$^+$ demonstrated the longest burst duration, with an average of 43 ms. By contrast, when probed using NB, the condensates formed by Aro$^-$ show an average duration of 26 ms (Fig. 4b). Note that although dense phase concentrations of proteins change minimally within the condensates formed by different variants[2,11,27], the simulations suggest that the extents of crosslinking vary with the number (valence) of aromatic residues[11,31]. Simulations show that the numbers of sticker–sticker interactions are highest in condensates formed by Aro$^+$ and lowest in condensates formed by Aro$^-$ (Fig. 4c). Thus, we infer that the longer burst durations for NB in Aro$^+$ condensates are due to the higher valence of aromatic residues. This larger valence results in higher extents of physical crosslinking and longer-lasting nanoscale hubs that trap NB for longer times and lead to longer fluorescence bursts. In contrast, condensates formed by Aro$^-$ feature fewer sticker–sticker interactions, leading to lower affinities and shorter burst durations when the condensates are probed using NB. Similar data were obtained when the condensates were probed using NR (Extended Data Fig. 6).

Dynamics can also be probed by measuring the speeds of fluorogen displacements. The measured speeds serve as useful proxies for evaluating how the mobilities of fluorogens are impeded by crosslinks, which generate locally elastic networks[31,53]. Our single-molecule tracking measurements indicate that NR moves fastest in Aro$^-$ condensates, with an average speed of 8.9 nm ms^{-1}. By contrast, NR moves most slowly in Aro$^+$ condensates, with an average speed of 6.7 nm ms^{-1} (Fig. 4d). These observations are in line with findings from LaSSI simulations[11,54], which show that proteins in Aro$^+$ condensates have the smallest displacements and proteins in Aro$^-$ condensates have the largest displacements (Fig. 4e and Extended Data Fig. 7).

Imaging the interfacial features of condensates

The fluorescence of MC540 is influenced by the molecular organization of the local environment[55,56]. We leveraged polarized epifluorescence microscopy to probe the orientational preferences sensed by this fluorogen (Methods). Condensates formed by Aro$^+$ exhibited discernible red and blue hues at the interfaces of condensates, indicating a strong polarization preference at the interface (Fig. 5a). Comparing Aro$^+$ with Aro$^-$ and wild-type A1-LCD, we note that the linear dichroism (Methods) distribution for Aro$^+$ is broader and encompasses more instances with large absolute linear dichroism values (Fig. 5b).

https://doi.org/10.1038/s41567-025-02827-7

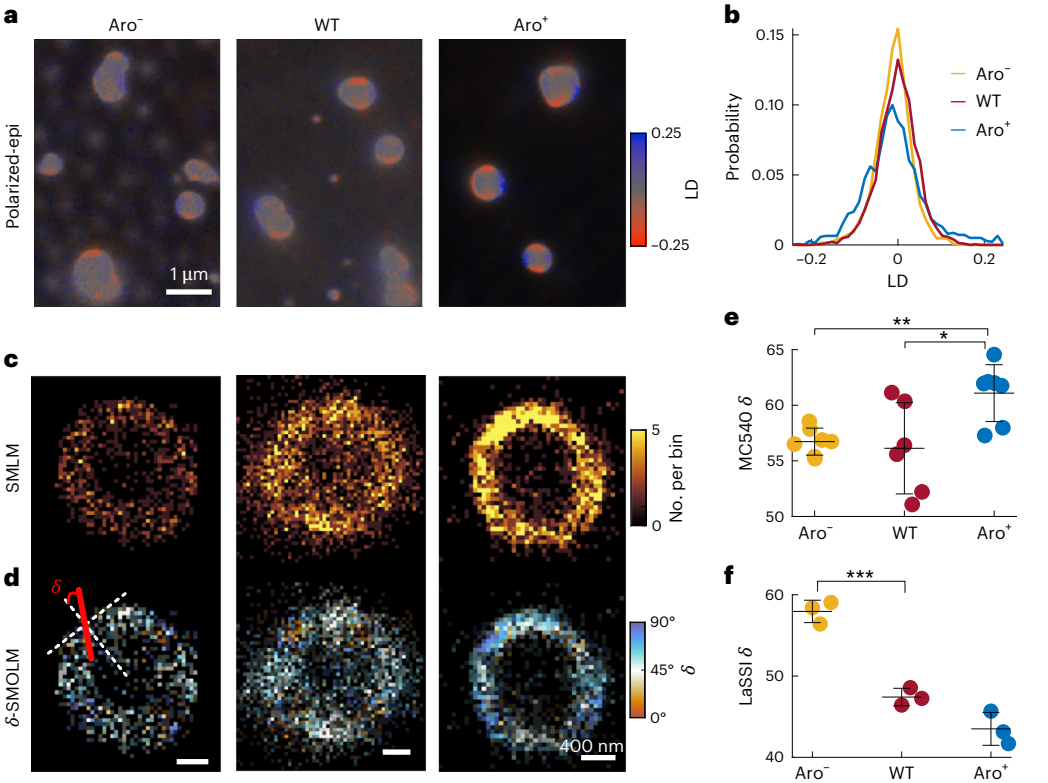

Fig. 5 | MC540 displays distinct orientations at interfaces, influenced by the numbers of aromatic residues. a, Colour-coded linear dichroism (LD) of MC540 within Aro⁻, A1-LCD (WT) and Aro⁺ variants, measured by polarized epifluorescence imaging. **b**, Linear dichroism distributions quantified from images shown in **a**. Yellow, Aro⁻; red, WT; blue, Aro⁺. **c**, SMLM images of MC540. **d**, Orientation angles δ for MC540 measured with respect to the normal vector to the condensate interface using SMOLM; the median angle δ is depicted within each 50-nm × 50-nm bin. **e**, Median δ values computed across individual condensates (circles). Here, seven Aro⁻ (520 ± 75 (mean ± s.d.) localizations each), six WT (1,310 ± 703 localizations each) and seven Aro⁺ (2,170 ± 943 localizations each) condensates across three biological replicates were used to derive mean (centre lines) ± s.d. (error bars). $P_{\text{Aro}^-,\text{Aro}^+} = 00.31$. **f**, δ values computed from LaSSI simulations using orientations of protein molecules at the interface (three independent simulations per condensate type). $P_{\text{Aro}^-,\text{WT}} = 6.36 \times 10^{-4}$. $^*P < 0.05$, $^{**}P < 0.01$, $^{***}P < 10^{-3}$. All P values were calculated using Welch's unequal variances t-test (two-sided).

Although SMLM images show a high density of MC540 at the interface of LCD condensates (Fig. 5c), they do not provide insights into how MC540 binds to the proteins. Thus, we employed SMOLM (Methods) for measuring both the three-dimensional position and the orientation of MC540 (Extended Data Fig. 8 and Supplementary Video 5). We quantified orientational preferences by quantifying the angle, denoted as δ, of MC540 in relation to the normal vector to the condensate interface (Fig. 5d). The SMOLM images, colour-coded according to δ and referred to as δ-SMOLM, indicate that freely diffusing MC540 dyes have a statistically significant preference for orientations parallel to the condensate interface (depicted in bluish hues in Fig. 5d). This orientational preference is observed at the interfaces of all three PLCD condensates (Fig. 5d). When comparing the median δ values across multiple condensates for the three LCD variants, we observed that Aro⁺ exhibits the highest δ value, with a mean of 61°, whereas Aro⁻ and wild-type A1-LCD have similar mean values of δ, which are 57° and 56°, respectively (Fig. 5e).

Scaffolds show statistical preferences for orientations perpendicular to the plane of the interface, and adsorbents show a statistical preference for orientations parallel to condensate interfaces[57]. MC540 may be viewed as an adsorbent, and the PLCD molecules are the scaffolds[57]. Unlike the adsorbents, scaffolds should have a statistical preference for perpendicular orientations. This expectation was confirmed using results from LaSSI simulations[11], which show that scaffold molecules have smaller δ values (Fig. 5f and Extended Data Fig. 9). The observed orientational preferences become more pronounced as the interactions among scaffolds become stronger with increasing numbers of aromatic residues (Fig. 5f). Taken together with the simulation results, the SMOLM data highlight the unique interfacial features of condensates.

Condensates as spatially inhomogeneous network fluids

The picture that emerges from single-fluorogen imaging is summarized in Fig. 6. The interiors of condensates are, on average, more hydrophobic than the coexisting dilute phases. Within condensates, spatial inhomogeneities are manifest as nanoscale hubs, and the fluorogens bind preferentially to hubs than the background of the condensate. SMOLM suggests that the interface between dilute and dense phases is a unique environment where MC540 molecules show marked orientational preferences that are more pronounced when the intermolecular interactions are stronger. Inhomogeneities on the micron scale have been established for stress granules[58], nucleoli[59], nuclear speckles[60] and the mitochondrial nucleoid[10]. Our work shows that nanoscale spatial inhomogeneities are also present, thus giving condensates their sponge-like appearance[61].

Other archetypes of LCDs that are drivers of condensate formation include RG-rich IDRs such as the N-terminal domain from the RNA helicase DDX4 (refs. 3,28) (Extended Data Fig. 10). Although the molecular grammars of RG-rich IDRs are different from those of PLCDs[11], these domains appear to form condensates that respond in similar ways to NB and NR. This similarity is not surprising given recent findings regarding the π-character[62] and their apparent hydrophobicity or arginine[63] as probed by how water molecules organize around arginine sidechains[64].

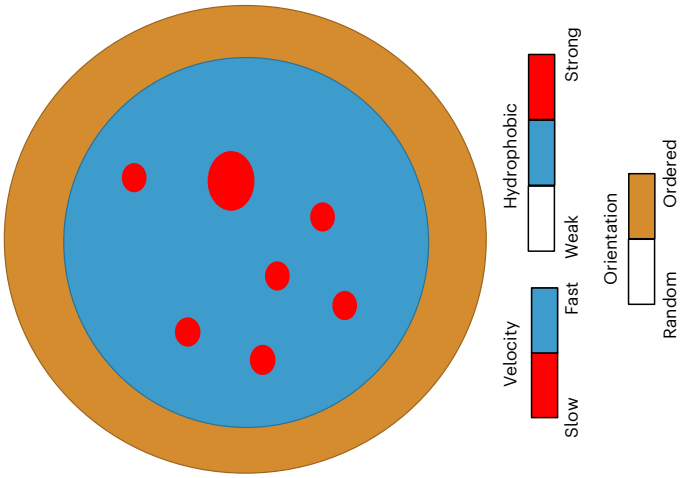

Fig. 6 | Schematic summarizing the structural features of condensates that were inferred from the fluorogenic experiments. Condensates are, on average, more hydrophobic than their coexisting dilute phases. They feature spatial inhomogeneities that are manifest as nanoscale hubs (red regions). Hubs are more hydrophobic compared to other regions (blue) within condensates, as well as to the dilute phase (white area). Fluorogens bound to nanoscale hubs move more slowly compared to other regions. Proteins at the interface (orange) have distinct orientational preferences that are unmasked by specific fluorogens such as MC540.

However, and in contrast to condensates formed by PLCDs and the RG-rich IDR of DDX4, the condensates formed by polynucleotides such as poly-rA respond very differently to NR (Extended Data Fig. 10). The implication is that different fluorogens, based on intercalation with nucleobases, are needed to probe the internal organization of RNA-rich condensates[57].

Previous studies based on partitioning small molecules suggest that condensates have distinct chemical environments[32–34]. Our findings indicate that partitioning data must be re-analysed through the lens of nanoscale spatial inhomogeneities within condensates. This will require adaptations of inhomogeneous fluid solvation theories[65]. In addition to necessitating a rethinking about partitioning data, our observations provide a structural and dynamical rationalization of reports of condensate viscoelasticity[4–6,8,9,29,31,66–68].

The continued development of new dye functionalities[69,70], imaging hardware[71] and analytical tools[72] will help with uncovering spatiotemporal organization and dynamics within condensates, including complex, multicomponent systems, thus enabling direct assessments of structure–function relationships of biomolecular condensates.

Online content

Any methods, additional references, Nature Portfolio reporting summaries, source data, extended data, supplementary information, acknowledgements, peer review information; details of author contributions and competing interests; and statements of data and code availability are available at https://doi.org/10.1038/s41567-025-02827-7.

References

1. Banani, S. F., Lee, H. O., Hyman, A. A. & Rosen, M. K. Biomolecular condensates: organizers of cellular biochemistry. *Nat. Rev. Mol. Cell Biol.* **18**, 285–298 (2017).
2. Bremer, A. et al. Deciphering how naturally occurring sequence features impact the phase behaviours of disordered prion-like domains. *Nat. Chem.* **14**, 196–207 (2022).
3. Nott, T. J. et al. Phase transition of a disordered nuage protein generates environmentally responsive membraneless organelles. *Mol. Cell* **57**, 936–947 (2015).
4. Jawerth, L. et al. Protein condensates as aging Maxwell fluids. *Science* **370**, 1317–1323 (2020).
5. Ghosh, A., Kota, D. & Zhou, H.-X. Shear relaxation governs fusion dynamics of biomolecular condensates. *Nat. Commun.* **12**, 5995 (2021).
6. Alshareedah, I., Moosa, M. M., Pham, M., Potoyan, D. A. & Banerjee, P. R. Programmable viscoelasticity in protein-RNA condensates with disordered sticker-spacer polypeptides. *Nat. Commun.* **12**, 6620 (2021).
7. Feric, M. et al. Coexisting liquid phases underlie nucleolar subcompartments. *Cell* **165**, 1686–1697 (2016).
8. Bergeron-Sandoval, L. P. et al. Endocytic proteins with prion-like domains form viscoelastic condensates that enable membrane remodeling. *Proc. Natl Acad. Sci. USA* **118**, e2113789118 (2021).
9. Alshareedah, I. et al. Sequence-specific interactions determine viscoelastic moduli and aging dynamics of protein condensates. *Nat. Phys.* **20**, 1482–1491 (2023).
10. Feric, M. et al. Mesoscale structure–function relationships in mitochondrial transcriptional condensates. *Proc. Natl Acad. Sci. USA* **119**, e2207303119 (2022).
11. Farag, M. et al. Condensates formed by prion-like low-complexity domains have small-world network structures and interfaces defined by expanded conformations. *Nat. Commun.* **13**, 7722 (2022).
12. Farag, M., Borcherds, W. M., Bremer, A., Mittag, T. & Pappu, R. V. Phase separation of protein mixtures is driven by the interplay of homotypic and heterotypic interactions. *Nat. Commun.* **14**, 5527 (2023).
13. Shillcock, J. C., Lagisquet, C., Alexandre, J., Vuillon, L. & Ipsen, J. H. Model biomolecular condensates have heterogeneous structure quantitatively dependent on the interaction profile of their constituent macromolecules. *Soft Matter* **18**, 6674–6693 (2022).
14. Grimm, J. B., Heckman, L. M. & Lavis, L. D. in *Progress in Molecular Biology and Translational Science*, Vol. 113 (ed. Morris, M. C.) Ch. 1 (Academic, 2013).
15. Martinez, V. & Henary, M. Nile red and Nile blue: applications and syntheses of structural analogues. *Chemistry* **22**, 13764–13782 (2016).
16. Verkman, A. S. Mechanism and kinetics of merocyanine 540 binding to phospholipid membranes. *Biochemistry* **26**, 4050–4056 (1987).
17. Li, H. & Vaughan, J. C. Switchable fluorophores for single-molecule localization microscopy. *Chem. Rev.* **118**, 9412–9454 (2018).
18. Lew, M. D. et al. Three-dimensional superresolution colocalization of intracellular protein superstructures and the cell surface in live Caulobacter crescentus. *Proc. Natl Acad. Sci. USA* **108**, E1102–E1110 (2011).
19. Spehar, K. et al. Super-resolution imaging of amyloid structures over extended times by using transient binding of single thioflavin T molecules. *Chembiochem* **19**, 1944–1948 (2018).
20. Danylchuk, D. I., Moon, S., Xu, K. & Klymchenko, A. S. Switchable solvatochromic probes for live-cell super-resolution imaging of plasma membrane organization. *Angew. Chem. Int. Ed.* **58**, 14920–14924 (2019).
21. Ding, T., Wu, T., Mazidi, H., Zhang, O. & Lew, M. D. Single-molecule orientation localization microscopy for resolving structural heterogeneities between amyloid fibrils. *Optica* **7**, 602–607 (2020).
22. Lu, J., Mazidi, H., Ding, T., Zhang, O. & Lew, M. D. Single-molecule 3D orientation imaging reveals nanoscale compositional heterogeneity in lipid membranes. *Angew. Chem. Int. Ed.* **59**, 17572–17579 (2020).
23. Klymchenko, A. S. Solvatochromic and fluorogenic dyes as environment-sensitive probes: design and biological applications. *Acc. Chem. Res.* **50**, 366–375 (2017).

24. Hou, Y., Bardo, A. M., Martinez, C. & Higgins, D. A. Characterization of molecular scale environments in polymer films by single molecule spectroscopy. *J. Phys. Chem. B* **104**, 212–219 (2000).
25. Sackett, D. L., Knutson, J. R. & Wolff, J. Hydrophobic surfaces of tubulin probed by time-resolved and steady-state fluorescence of nile red. *J. Biol. Chem.* **265**, 14899–14906 (1990).
26. Tajalli, H., Gilani, A. G., Zakerhamidi, M. S. & Tajalli, P. The photophysical properties of Nile red and Nile blue in ordered anisotropic media. *Dyes Pigm.* **78**, 15–24 (2008).
27. Martin, E. W. et al. Valence and patterning of aromatic residues determine the phase behavior of prion-like domains. *Science* **367**, 694–699 (2020).
28. Brady, J. P. et al. Structural and hydrodynamic properties of an intrinsically disordered region of a germ cell-specific protein on phase separation. *Proc. Natl Acad. Sci. USA* **114**, E8194–E8203 (2017).
29. Alshareedah, I., Kaur, T. & Banerjee, P. R. Methods for characterizing the material properties of biomolecular condensates. *Methods Enzymol.* **646**, 143–183 (2021).
30. Kaur, T. et al. Sequence-encoded and composition-dependent protein-RNA interactions control multiphasic condensate morphologies. *Nat. Commun.* **12**, 872 (2021).
31. Cohen, S. R., Banerjee, P. R. & Pappu, R. V. Direct computations of viscoelastic moduli of biomolecular condensates. *J. Chem. Phys.* **161**, 095103 (2024).
32. Kilgore, H. R. et al. Distinct chemical environments in biomolecular condensates. *Nat. Chem. Biol.* **20**, 291–301 (2023).
33. Kilgore, H. R. & Young, R. A. Learning the chemical grammar of biomolecular condensates. *Nat. Chem. Biol.* **18**, 1298–1306 (2022).
34. Thody, S. A. et al. Small molecule properties define partitioning into biomolecular condensates. *Nat. Chem.* **16**, 1794–1802 (2022).
35. King, M. R. et al. Macromolecular condensation organizes nucleolar sub-phases to set up a pH gradient. *Cell* **187**, 1889–1906.e1824 (2024).
36. Posey, A. E. et al. Biomolecular condensates are characterized by interphase electric potentials. *J. Am. Chem. Soc.* **146**, 28268–28281 (2024).
37. Nott, T. J., Craggs, T. D. & Baldwin, A. J. Membraneless organelles can melt nucleic acid duplexes and act as biomolecular filters. *Nat. Chem.* **8**, 569–575 (2016).
38. Sharonov, A. & Hochstrasser, R. M. Wide-field subdiffraction imaging by accumulated binding of diffusing probes. *Proc. Natl Acad. Sci. USA* **103**, 18911–18916 (2006).
39. Ruff, K. M., Dar, F. & Pappu, R. V. Ligand effects on phase separation of multivalent macromolecules. *Proc. Natl Acad. Sci. USA* **118**, e2017184118 (2021).
40. Ruff, K. M., Dar, F. & Pappu, R. V. Polyphasic linkage and the impact of ligand binding on the regulation of biomolecular condensates. *Biophys. Rev.* **2**, 021302 (2021).
41. Kuo, C. & Hochstrasser, R. M. Super-resolution microscopy of lipid bilayer phases. *J. Am. Chem. Soc.* **133**, 4664–4667 (2011).
42. Lelek, M. et al. Single-molecule localization microscopy. *Nat. Rev. Methods Primers* **1**, 39 (2021).
43. Betzig, E. et al. Imaging intracellular fluorescent proteins at nanometer resolution. *Science* **313**, 1642–1645 (2006).
44. Hess, S. T., Girirajan, T. P. K. & Mason, M. D. Ultra-high resolution imaging by fluorescence photoactivation localization microscopy. *Biophys. J.* **91**, 4258–4272 (2006).
45. Rust, M. J., Bates, M. & Zhuang, X. Sub-diffraction-limit imaging by stochastic optical reconstruction microscopy (STORM). *Nat. Methods* **3**, 793–796 (2006).
46. Chhabra, R. Nonwoven uniformity—measurements using image analysis. *Int. Nonwovens J.* **os-12**, 1558925003os-1200112 (2003).
47. Ripley, B. D. Modelling spatial patterns. *J. R. Stat. Soc.* **39**, 172–192 (1977).
48. Khater, I. M., Nabi, I. R. & Hamarneh, G. A review of super-resolution single-molecule localization microscopy cluster analysis and quantification methods. *Patterns* **1**, 100038 (2020).
49. Malkusch, S. et al. Coordinate-based colocalization analysis of single-molecule localization microscopy data. *Histochem. Cell Biol.* **137**, 1–10 (2012).
50. Shen, M. et al. Nanoscale colocalization of fluorogenic probes reveals the role of oxygen vacancies in the photocatalytic activity of tungsten oxide nanowires. *ACS Catal.* **10**, 2088–2099 (2020).
51. Shen, Z. et al. Biological condensates form percolated networks with molecular motion properties distinctly different from dilute solutions. *eLife* **12**, e81907 (2023).
52. Dar, F. et al. Biomolecular condensates form spatially inhomogeneous network fluids. *Nat. Commun.* **15**, 3413 (2024).
53. Weeks, E. R. & Weitz, D. A. Properties of cage rearrangements observed near the colloidal glass transition. *Phys. Rev. Lett.* **89**, 095704 (2002).
54. Choi, J.-M., Dar, F. & Pappu, R. V. LASSI: a lattice model for simulating phase transitions of multivalent proteins. *PLoS Comput. Biol.* **15**, e1007028 (2019).
55. Kulinich, A. V. Aleksandr AI. Merocyanine dyes: synthesis, structure, properties and applications. *Russ. Chem. Rev.* **78**, 141–164 (2009).
56. Stillwell, W. et al. Use of merocyanine (MC540) in quantifying lipid domains and packing in phospholipid vesicles and tumor cells. *Biochim. Biophys. Acta Biomembr.* **1146**, 136–144 (1993).
57. Erkamp, N. A. et al. Differential interactions determine anisotropies at interfaces of RNA-based biomolecular condensates. Preprint at *bioRxiv* https://doi.org/10.1101/2024.08.19.608662 (2024).
58. Jain, S. et al. ATPase-modulated stress granules contain a diverse proteome and substructure. *Cell* **164**, 487–498 (2016).
59. Pederson, T. The nucleolus. *Cold Spring Harb. Perspect. Biol.* **3**, a000638 (2011).
60. Fei, J. et al. Quantitative analysis of multilayer organization of proteins and RNA in nuclear speckles at super resolution. *J. Cell Sci.* **130**, 4180–4192 (2017).
61. Handwerger, K. E., Cordero, J. A. & Gall, J. G. Cajal bodies, nucleoli, and speckles in the xenopus oocyte nucleus have a low-density, sponge-like structure. *Mol. Biol. Cell* **16**, 202–211 (2005).
62. Vernon, R. M. et al. Pi-Pi contacts are an overlooked protein feature relevant to phase separation. *eLife* **7**, e31486 (2018).
63. Hong, Y. et al. Hydrophobicity of arginine leads to reentrant liquid-liquid phase separation behaviors of arginine-rich proteins. *Nat. Commun.* **13**, 7326 (2022).
64. Fossat, M. J., Zeng, X. & Pappu, R. V. Uncovering differences in hydration free energies and structures for model compound mimics of charged side chains of amino acids. *J. Phys. Chem. B* **125**, 4148–4161 (2021).
65. Huggins, D. J. Application of inhomogeneous fluid solvation theory to model the distribution and thermodynamics of water molecules around biomolecules. *Phys. Chem. Chem. Phys.* **14**, 15106–15117 (2012).
66. Zhou, H.-X. Viscoelasticity of biomolecular condensates conforms to the Jeffreys model. *J. Chem. Phys.* **154**, 041103 (2021).
67. Alshareedah, I. et al. Determinants of viscoelasticity and flow activation energy in biomolecular condensates. *Sci. Adv.* **10**, eadi6539 (2024).
68. Wróbel, J. K., Cortez, R. & Fauci, L. Modeling viscoelastic networks in Stokes flow. *Phys. Fluids* **26**, 113102 (2014).
69. Needham, L.-M. et al. ThX – a next-generation probe for the early detection of amyloid aggregates. *Chem. Sci.* **11**, 4578–4583 (2020).

70. Aparin, I. O. et al. Fluorogenic dimers as bright switchable probes for enhanced super-resolution imaging of cell membranes. *J. Am. Chem. Soc.* **144**, 18043–18053 (2022).
71. Zhang, O. et al. Six-dimensional single-molecule imaging with isotropic resolution using a multi-view reflector microscope. *Nat. Photonics* **17**, 179–186 (2023).
72. Schröder, T. et al. Shrinking gate fluorescence correlation spectroscopy yields equilibrium constants and separates photophysics from structural dynamics. *Proc. Natl Acad. Sci. USA* **120**, e2211896120 (2023).

Methods

Sample preparation

Expression and purification of A1-LCD. BL21-CODONPlus RIPL *Escherichia coli* cells (Agilent Technologies, 230280) transfected with Δhexa_His-TEV-A1-LCD (wild-type, Aro$^-$ or Aro$^+$)[27] were grown in LB broth (Sigma, L3522) in Erlenmeyer flasks with ≥ 5-fold head volume at 37 °C and 220 rotations per minute orbital shaking until optical density at a wavelength of 600 nm of ~0.6 was reached. Cultures were then chilled for 15 min in an ice bath before being induced with 0.35 mM IPTG. Expression-induced cultures were grown for 6 h at 37 °C. Cells were harvested by centrifugation, washed of residual media, flash frozen and stored as pellets in 50-ml Falcon tubes at −80 °C.

At the start of purification, the cell pellet was gently resuspended to homogeneity in 35 ml supplemented lysis buffer (50 mM MES, 500 mM NaCl, 14.3 mM BME (β-mercaptoethanol), 200 µM PMSF (phenylmethylsulfonyl fluoride); pH 6). Lysis buffer supplements are 500U DNAaseI (Sigma, 4536282001), 500U RNAse A (Sigma, 10109169001), 5 mg lysozyme (Sigma, 62971-10G-F) and one protease inhibitor tablet (Sigma, 40694200). The cell suspension was lysed via sonication on a Branson 550 sonicator with an L102C horn attachment using five series of the following 20-round cycle: 1 s on/2 s off at 30% power. After a 30-min spin at 38,000*g*, the pellet was resuspended in a resuspension buffer (6 M GdmCl, 20 mM Tris, 15 mM imidazole, 14.3 mM BME and 200 µM PMSF; pH 7.5) via repeat pipetting and pulses of sonication until the solution was visibly homogenous. This solubilized pellet was spun at 38,000*g* for 30 min, and the supernatant was applied to a gravity column with 5 ml bed volume of HiPur NiNTA resin (Fisher, 88223) equilibrated with resuspension buffer. The NiNTA resin was washed in 75 ml wash buffer (20 mM Tris, 30 mM ImZ, 4 M urea, 14.3 mM BME and 200 µM PMSF; pH 7.5), and then protein was eluted in elution buffer (20 mM Tris, 350 mM ImZ, 4 M urea, 14.3 mM BME and 200 µM PMSF; pH 7.5). Peak fractions from NiNTA affinity purification were pooled and diluted 1:1 in dilution buffer (20 mM Tris and 14.3 mM BME; pH 7.5). To this, 1 mg of TEV protease was added, and the mixture was dialysed overnight in dialysis buffer (20 mM Tris, 2 M urea, 50 mM NaCl, 0.5 mM EDTA and 1 mM dithiothreitol; pH 7.5). The following morning, the protein solution was filtered through a 0.22-µm filter and then further purified via ion-exchange chromatography on an ÄKTA Pure fast protein liquid chromatography (FPLC) module using a HiTrap SP 5 ml column (Cytiva, 17115201). The column was equilibrated with buffer A (20 mM Tris, 2 M urea, 50 mM NaCl and 14.3 mM BME; pH 7.5), and protein was bound and then subjected to a continuous gradient protocol from 0.05 M NaCl to 1 M NaCl. Fractions containing A1-LCD were pooled and then further purified and buffer exchanged using size-exclusion chromatography (HiLoad 16/600 Superdex 200 pg column (Cytiva, 28989335)) into the following storage buffer: 20 mM MES and 4 M GdmCl at pH 5.5. Finally, protein was pooled and concentrated in Amicon Ultra 3 molecular weight cut-off concentrator columns (Millipore-Sigma UFC, 500396) according to the manufacturer's suggestions. Concentrated protein was stored at 4 °C until used.

Expression and purification of DDX4-NT. BL21 *E. coli* cells (NEB, C2530H) transfected with His-SUMO-DDX4-NT[28], a gift from L. E. Kay, were grown in the same manner as A1-LCD. Cells were lysed in the same manner as A1-LCD, with the only difference being the supplemented lysis buffer (20 mM sodium phosphate, 750 mM NaCl, 20 mM imidazole, 14.3 mM BME and 0.2 mM PMSF; pH 7.5). The supernatant was recovered from a 25-min spin at 38,000*g* and bound to an equilibrated HisTrap FF Crude 5 ml column (Cytiva, catalogue no. 11000458) using an ÄKTA Pure FPLC module. The NiNTA column was washed in 75 ml lysis buffer, and then protein was eluted in elution buffer (0.02 M sodium phosphate, 0.5 M NaCl, 0.35 M imidazole, 0.0143 M BME, 0.0002 M PMSF; pH 7.5). Peak fractions from this affinity purification were pooled and diluted 5-fold in dilution buffer (0.02 M sodium phosphate, 0.0143 M BME; pH 7.5). This solution was further purified via ion-exchange chromatography using a continuous gradient purification protocol with a HiTrap Heparin HP 5 ml column (Cytiva, 17040703), buffer A (0.02 M sodium phosphate, 0.1 M NaCl, 0.0143 M BME; pH 7.5) and buffer B (0.02 M sodium phosphate, 0.1 M NaCl, 0.0143 M BME; pH 7.5) on the ÄKTA Pure FPLC module. Peak fractions containing SUMO-DDX4 protein were pooled and cleaved of SUMO tags during an overnight dialysis in the presence of 0.02× ULP1 Protease in cleavage buffer (0.02 M sodium phosphate, 0.3 M NaCl, 0.001 M Dithiothreitol; pH 7.5). DDX4-NT was purified to ≥98% using size-exclusion chromatography: HiLoad 16/600 Superdex 200 pg column (Cytiva, 28989335) on the ÄKTA Pure FPLC module in storage buffer (0.022 M sodium phosphate, 1.1 M NaCl, 0.0143 M BME; pH 7.5). The DDX4-NT solution was supplemented with 10% glycerol and concentrated in Amicon Ultra 3 molecular weight cut-off concentrator columns (Millipore-Sigma UFC, 500396), and concentrated protein was aliquoted into single-use volumes (typically 10 µl), flash frozen in liquid N_2 and stored at −80 °C. Each step of the purification was assessed in the same manner as described for A1-LCD.

Assessing protein purity. After each stage of purification (affinity, ion exchange, size exclusion and concentration steps), protein concentration and nucleotide levels were assessed on a Nanodrop2000 via absorbance at 280-nm measurements (A280) and A260/A280 ratiometric measurements. Similarly, after each purification stage, the inputs, flow-throughs, washes and elutes were interrogated using sodium dodecyl sulfate–polyacrylamide gel electrophoresis (gel, BioRad mini-PROTEAN TGX AnyKD, 4569036; MW latter, BioRad Precession Plus Protein Standard Unstained, 1610363), stained with EZblue Coomassie stain (10% (v/v) phosphoric acid, 10% (w/v) ammonium sulfate, 20% (v/v) methanol, 1.2% (w/v) Coomassie blue) and destained via serial washes in ddH_2O. All proteins were purified to ≥99% purity assessed by densitometry of the Coomassie stained gels. Furthermore, all proteins exhibited an A260/A280 ratio of <0.65, indicating no detectable nucleotide contamination.

Preparation of condensates for imaging. We adhered a silicone isolator (Grace Bio-labs, SKU 665206) to coverglass (Azer Scientific, ES0107242, high precision 1.5H, 24 mm × 60 mm, 170 ± 5 µm) to create a small chamber for imaging. To induce phase separation, we mixed 9 µl of ~100 µM A1-LCD (in 20 mM HEPES buffer; pH 7.0) with 1 µl of aqueous buffer (20 mM HEPES buffer with 3 M NaCl; pH 7.0) into the chamber to a final concentration of ~90 µM A1-LCD in 20 mM HEPES buffer with 300 mM NaCl. We then immediately added 0.5 µl of a solution (20 mM HEPES buffer with 300 mM NaCl; pH 7.0) containing a fluorogenic probe (final concentrations shown in Supplementary Table 2) to the chamber. Phase separation occurs spontaneously within the chamber at room temperature (22 °C) to form condensates for imaging. We noticed that condensates made with mixtures of His-tagged A1-LCD and untagged A1-LCD did not completely wet the coverslip, permitting condensates to remain distinct and unfused. We therefore use untagged A1-LCD for the wetting experiment shown in Extended Data Fig. 3, whereas an A1-LCD mixture containing ~20% His-tagged A1-LCD was used for experiments requiring distinct condensates shown in Figs. 1–3. The value we measure for c_{sat} for the His-tagged wild-type A1-LCD is 90 ± 4.5 µM at ~20 °C. Under similar solution conditions and at precisely 20 °C, the measured c_{sat} for the untagged A1-LCD is 102 ± 4.7 µM. To put this in context, increasing the temperature by 2 °C increases c_{sat} to 124 ± 5.5 µM and decreasing it by 2 °C lowers c_{sat} to 77 ± 6 µM for the untagged A1-LCD. From the slope of the binodal that has been reported for A1-LCD, we infer that adding a His-tag is akin to lowering the temperature by 1°C. Because the measurements are made far away from the critical temperature ($T_c \approx 51$ °C), the condensates we image are expected be close facsimiles of the condensates formed by the untagged A1-LCD. Furthermore, we use a mixture comprising His-tagged A1-LCD (20%) and untagged A1-LCD (80%) for our imaging studies. Therefore, the driving forces for condensate formation are

dominated by the untagged rather than His-tagged molecules. An identical procedure was followed for preparing Aro^- and Aro^+ condensates shown in Figs. 4 and 5, with the only difference being that we used a mixed 9 µl of ~160 µM Aro^- A1-LCD to account for its lower saturation concentration (c_{sat}). To prepare DDX4 condensates for imaging, we mixed 1 µl of 2320 µM DDX4 (in 8 mM NaH_2PO_4, 12 mM Na_2HPO_4, 0.75 M NaCl) with 9 µl low-salt solution (8 mM NaH_2PO_4, 12 mM Na_2HPO, 0 M NaCl) in a small chamber for imaging.

Preparation of condensates to measure driving forces for phase separation. Driving forces were quantified by measuring saturation concentrations (c_{sat}) of A1-LCD molecules in the presence of different concentrations of fluorogens used in this work (Supplementary Table 2). For each sample, we induced phase separation, incubated the sample at a given temperature for 30 min and then separated the dilute phase from the dense phase via centrifugation at 14,000*g* for 15 s. We then measured the protein concentration of the dilute phase. This is a standard assay for measuring c_{sat} because the dilute phase concentration is the c_{sat} that equalizes the chemical potential of the dense and dilute phases across the phase boundary. We mixed 42.5 µl of ~175 µM A1-LCD (in 20 mM HEPES buffer; pH 7.0) with 5 µl of salt buffer (20 mM HEPES buffer with 3 M NaCl; pH 7.0) and 2.5 µl of a fluorogenic solution (20 mM HEPES buffer with 300 mM NaCl; pH 7.0) all at once in a low-protein-retention Eppendorf tube (Fisher, 11535564). The final concentration of A1-LCD was ~150 µM, and the final concentration of dye was matched to those used in the imaging experiments (Supplementary Table 2); final solution conditions were 20 mM HEPES buffer with 300 mM NaCl. Each condition shown in Extended Data Fig. 2 was prepared three times in parallel. Prepared protein and dye mixtures were allowed to phase separate for 30 min at either 23 °C or 4 °C before the mixture was centrifuged, at its incubation temperature, at 14,000*g* for 30 s. Then, 10 µl of the resultant dilute phase was recovered, and protein concentration was measured using absorbance at 280 nm on a Nanodrop2000.

Optical microscope setup and imaging procedure

Optical setup. We used a home-built inverted microscope for epifluorescence imaging, single-molecule imaging, single-molecule tracking (Supplementary Fig. 1a), polarized epifluorescence and single-molecule orientation imaging (Supplementary Fig. 1b). The microscope is equipped with an oil-immersion objective (Olympus UPLSAPO100XOPSF, NA 1.4). The excitation laser, dichroic mirror and emission filters were switched to match the excitation and emission spectra of NB, NR and MC540 (Supplementary Table 3). A relatively low peak laser intensity (~51 W cm^{-2}) and high concentration of fluorogens were used for epifluorescence imaging (Supplementary Table 2). A relatively large peak laser intensity ~4,088 W cm^{-2} coupled with ultra-low concentrations of fluorogens facilitates bright fluorescence flashes for single-molecule imaging, tracking and orientation measurement. Fluorescence images were acquired by a Photometrics Prime BSI sCMOS camera controlled via Micro-Manager (v.2.0.3).

Polarization-sensitive epifluorescence imaging. We separate the fluorescence emission from MC540 into *x*- and *y*-polarized channels (I_x, I_y). We then calculate linear dichroism as the ratio $(I_x - I_y)/(I_x + I_y)$, which takes values from −1 to +1. A linear dichroism value near +1 signifies that the *x* polarization dominates the fluorescence emission, whereas a negative linear dichroism value near −1 indicates dominance of *y* polarization.

Single-molecule orientation-localization measurement. For measuring the orientation of MC540 in condensates, we use the pixOL microscope, which enables three-dimensional position and three-dimensional orientation measurement simultaneously[73] (Supplementary Fig. 1b,c). The pixOL microscope is designed to show different dipole-spread functions on the camera, depending on the orientation and three-dimensional position of MC540 (Supplementary Fig. 1d–f).

Imaging protocols using multiple fluorogenic probes. Because the emission and excitation spectra of MC540 and NB are well separated, we imaged single condensates using multiple probes by switching the excitation laser, dichroic mirror and emission filter appropriately without crosstalk (Supplementary Table 3). However, there is crosstalk between the emission spectra of NB and NR. The emission spectrum of NR significantly overlaps with the red window of our microscope (676 ± 18 nm), whereas the emission of NB is barely observable in the orange window (593 ± 23 nm; Supplementary Fig. 4). Single NB molecules are virtually undetectable in the orange window (Supplementary Fig. 5). To image a single condensate using both NB and NR, we always captured NB images first in the absence of NR using the red-pass filter (Supplementary Table 3), where the solution containing A1-LCD and NB was prepared according to the procedure above and Supplementary Table 2. After NB imaging, we added 0.5 µl of a solution (20 mM HEPES buffer with 300 mM NaCl; pH 7.0) containing NR (final concentrations shown in Supplementary Table 2) to the chamber. NR within the condensates was then imaged using the orange-pass filter. We observed stable, consistent intensity values (epifluorescence imaging) and blinking dynamics (single-molecule imaging/tracking) for NR within seconds of adding it to the imaging chamber.

Confocal imaging. Point-scanning confocal microscopy was carried out on a Leica STELLARIS 8 FELCON confocal microscope equipped with a white-light laser and adjustable band pass emission filters. This setup allowed imaging under the same excitation and emission wavelengths as those used in the custom-built microscope (see parameters for NR and NB in Supplementary Table 3). Samples were prepared as described in the 'Preparation of condensates for imaging' section, and concentrations of dyes matched to those used for epifluorescence imaging (Supplementary Table 2). These samples were imaged using a ×100 oil-immersion HC PL APO objective (1.40 NA) and a Leica Power HyD R detector. *Z* stacks were taken in 0.5 µm intervals from the coverslip surface up to at least 7 µm above this point. Images of stacks were taken sequentially using DIC/brightfield illumination followed by confocal imaging and at 8-bit depth. These image stacks were saved as TIFFs.

Statistics and reproducibility

No statistical method was used to predetermine sample size. At least three condensates per field of view and three fields of view per independent experiment were observed/measured for consistency. Single-molecule statistics utilize 500–10^5 localizations per condensate, depending on the experiment, which enables reliable calculations of means, medians and standard deviations as necessary. All micrographs (for example, DIC and confocal images in Fig. 1d,f and polarized epifluorescence images in Fig. 5a, Extended Data Figs. 1, 3, 5 and 10 and Supplementary Figs. 4 and 5) are representative of greater than three independent experiments / biological replicates. No data were excluded from the analyses except when filtering or thresholds were applied during image analysis as detailed below. All experiments were repeated a minimum of three times using independent preparations. Biological replicates are defined as condensates that are prepared either from batches of protein that have been purified from distinct bacterial expressions or condensates that have been prepared from a stock of protein that is kept in long-term storage for up to 6 months. Data collection and experimental conditions were not randomized. Data collection and analysis were not performed blind to the conditions of the experiments. All *P* values were calculated using Welch's unequal variances *t*-test (two-sided); for these tests, the data distribution was assumed to be normal, but this was not formally tested.

Data analysis

Single-molecule detection and estimation algorithm. SMLM depends on sequential detection and localization of individual molecular

blinking events. These events are stochastic, and ref. 74 developed a bespoke regularized maximum-likelihood estimation algorithm, termed the robust statistical estimation (RoSE) algorithm, to robustly analyse frames containing a high density of active molecules, or molecules whose images overlap. This algorithm minimizes biases by jointly estimating the number and positions of blinking events to localize molecules more accurately and eliminate false localizations. We used RoSE[74] to estimate single-molecule positions, brightness and fluorescence burst durations. A regularization parameter of 0.3 and a calibrated point-spread function[75] model were used for estimation to account for optical aberrations. Details of the RoSE algorithm have been published and are not reproduced here. See the 'Code Availability' statement[76].

Single-molecule orientation estimation. Single-molecule orientation measurement requires detection of fluorescence 'flashes' within raw camera images and estimating their three-dimensional positions and orientations based on the shape of the 'flashes'. We use a bespoke maximum-likelihood estimator, RoSEO3D, to estimate the orientation and three-dimensional position as described by ref. 73. See the 'Code availability' statement[76].

Calculating the orientation angle δ. To calculate the orientation angle for MC540 measured with respect to the normal vector to the condensate interface, we first fit the estimated three-dimensional condensate structure to an ellipsoid (Supplementary Fig. 7). The normal vector to the condensate interface is calculated based on the surface of fitted ellipsoid. Next, we calculate the angle δ between the estimated orientation $[\theta,\phi]$ and the surface normal. For comparing the orientation δ among three A1-LCD variants shown in Fig. 5e, we only consider emitters with high estimation precision, namely emitters with a signal count larger than 500 photons, with polar angle θ larger than 60° and with axial positions h in [100, 800] nm. These filters ensure precise and reliable measurements of δ because dim molecules high above the coverslip are more difficult to measure.

Single-molecule tracking analysis grouping localizations and quantifying burst durations and displacement trajectories. At low concentrations of fluorogens, emitters are sparse enough to be easily distinguishable from one another. Two localizations are classified as originating from a single emitter if they appear within two adjacent camera frames and are separated by a distance smaller than a threshold $T = 175 + 4\sigma_r$ nm, where σ_r is the localization precision that varies for emitters with different signal-to-background ratios (~15 nm on average). Localizations collected at 10-ms intervals (the exposure time of the camera) are grouped together into a single trajectory until an emitter becomes dark: namely, when all emitters in the next frame are separated by a distance $>T$ from the current emitter. The burst duration of a fluorescence emitter is equal to $N_f \times 10$ ms, where N_f is the number of frames in the trajectory (Fig. 3b). The speed of an emitter is calculated as the Euclidean distance between its positions in each pair of consecutive frames within a trajectory (Fig. 3e,h,i); if the trajectory is longer than two frames, then each speed, calculated from a pair of frames, is reported separately (for example, in Fig. 3e).

Quantifying the degree of clustering within each condensate. The clustering coefficient is calculated for each localization based on Ripley's $H(r)$ and Getis and Franklin's $L(r)$ functions[47,48]. To assign a cluster coefficient to the ith localization p_i, we define a circular region centred at p_i with a radius r of 50 nm. The radius r is chosen to be larger than the localization precision, ~15 nm, of SMLM. This choice also ensures against blurring out the local information. The number of single molecules within this circular region is used to quantify

$$H(r) = \sqrt{\frac{N_{p_i}}{\lambda\pi}} - r \tag{1}$$

Here, N_{p_i} represents the number of SMs within the circular region, and λ is the average localization density across each condensate. The cluster coefficient quantifies how clustered or dispersed the measured distribution is when compared to a uniform distribution. Localizations are classified as clustered if $H(r)$ is above some threshold (for example, 20 in Fig. 2e).

Excess variance. We note that if single-molecule localizations are described by a homogenous Poisson process, otherwise referred to as complete spatial randomness, then we expect the mean localization density to match the variance of the localization density when both statistics are calculated across an entire condensate or multiple condensates. Thus, the heterogeneity of localizations within a condensate may be quantified using excess variance, defined as

$$V = \frac{\text{variance}\,(S_{\text{con}})}{\text{mean}\,(S_{\text{con}})} - 1 \tag{2}$$

Here, S_{con} represents a collection of localization densities (per 20-nm × 20-nm bin) measured within a condensate. We expect a uniformly random distribution to have an excess variance of zero (Supplementary Fig. 3). An excess variance larger than zero represents heterogeneous structures.

Coordinate-based correlation between fluorogens. We quantified the colocalization between pairs of fluorogenic probes (A and B) directly using the position coordinates provided by SMLM rather than the brightness of pixels within an image[49]. To calculate the coordinate-based correlation (CBC) value for a specific localization A_i from dataset A, the distribution of localizations from both species A and B around A_i is calculated as

$$D_{A_i,A}(r) = \frac{N_{A_i,A}(r)}{N_{A_i,A}(R_{\max})}\frac{R_{\max}^2}{r^2} \tag{3}$$

$$D_{A_i,B}(r) = \frac{N_{A_i,B}(r)}{N_{A_i,B}(R_{\max})}\frac{R_{\max}^2}{r^2} \tag{4}$$

where $N_{A_i,A}(r)$ and $N_{A_i,B}(r)$ are the number of localizations of species A and species B within the distance r around A_i, respectively. In our calculation, we set $R_{\max}$ to be 300 nm, which determines the size of the region over which correlations are calculated. We then calculate the rank correlation coefficient as

$$S_{A_i} = \frac{\sum_{r_j=0}^{R_{\max}}\left(O_{D_{A_i,A}}(r_j) - \bar{O}_{D_{A_i,A}}\right)\left(O_{D_{A_i,B}}(r_j) - \bar{O}_{D_{A_i,B}}\right)}{\sqrt{\left(\sum_{r_j=0}^{R_{\max}}\left(O_{D_{A_i,A}}(r_j) - \bar{O}_{D_{A_i,A}}\right)^2\right)}\sqrt{\left(\sum_{r_j=0}^{R_{\max}}\left(O_{D_{A_i,B}}(r_j) - \bar{O}_{D_{A_i,B}}\right)^2\right)}} \tag{5}$$

where $O_{D_{A_i,A}}$ is the rank of $D_{A_i,A}$, and $\bar{O}_{D_{A_i,A}}$ is the mean of $O_{D_{A_i,A}}$. The CBC value of A_i is calculated using

$$\text{CBC}_{A_i} = S_{A_i}\exp\left(-\frac{E_{A_i,B}}{R_{\max}}\right) \tag{6}$$

with $E_{A_i,B}$ as the distance from A_i to the nearest neighbour from species B. CBC values range from −1 to 1.

Analysis of confocal images. Condensates were imaged as a confocal Z stack. All images shown are of a single Z slice that is representative and 1.5 µm above the coverslip; brightness and contrast have been optimized. Line scans were carried out using the line tool and plot profile analysis in ImageJ (v.14.0/1.54f). Line thickness was set to

3 pixels, and the same length of line was drawn through five condensates per condition (NR and NB). Condensates were analysed if they had equivalent diameters. The resultant intensity profiles were used to obtain median and 95th percentile confidence interval values of dye intensity. Partition coefficients were determined as follows: using only Z slices 1.5 µm above the coverslips, coordinates of condensates were calculated via Otsu thresholding. Condensates smaller than 30 pixels (0.1411 µm per pixel) were omitted. Using the analyse particle tool, the mean intensity value (in arbitrary units (a.u.)) for individual condensates was saved as 'condensate signal'. To use these values to obtain partition coefficients (PCs), we carried out additional analysis as follows: an independent thresholding procedure was applied to duplicated images to obtain the aggregate intensity of all coordinates in the frame that fell outside the condensate signal that we term 'background'. Individual PCs are the difference of the condensate signal and background. PC values are reported as a normalized value, where 1 is the background.

LaSSI simulations

To provide a physical interpretation for why NR and NB dyes are trapped for longer periods of time at hubs, we analysed published results from lattice-based LaSSI simulations[11]. Interactions for A1-LCD and related PLCDs follow a hierarchy whereby interactions between aromatic residues are the strongest[11]. Aromatic residues of A1-LCD and related PLCDs function as stickers that enable physical crosslinking of these molecules[2,27]. Conversely, charged and polar residues interspersed between the stickers act as spacers[2,27]. The simulations of ref. 11 showed that the spatial inhomogeneity and network connectivity within PLCD condensates are governed by the valence of stickers[27] and differences in interaction strengths between different stickers and spacers[11].

Simulations were performed using LaSSI[54], a lattice-based Monte Carlo engine, as described previously[11]. Monte Carlo moves are accepted or rejected based on the Metropolis–Hastings criterion so that the probability of accepting a move is equal to $\min(1, \exp(-\beta\Delta E))$, where $\beta = 1/\mathrm{kT}$. Here, kT is the simulation temperature and ΔE is the change in total system energy associated with the attempted move. Total system energies were calculated using a nearest-neighbour model and previously derived interaction parameters, which have been shown to accurately capture the phase behaviour of A1-LCD and variants thereof[27]. For each simulation, 200 distinct chain molecules comprising 137 beads each were placed in a cubic lattice with a length of 120 lattice units. Previous calibrations have shown that the numbers of molecules used in these simulations are adequate to avoid problems due to finite size effects. The simulations were performed for 10^{12} Monte Carlo moves and were allowed to equilibrate such that the chains formed a single condensate with a coexisting dilute phase before any analysis was performed. Given our interest in the dynamics of the condensate chains, we limited the Monte Carlo move set to local moves, eliminating non-physical moves that are part of the total set of moves. The jumping distance of chains in the condensate was calculated by tracking the distance moved by the centre of mass of each chain after 2.5×10^8 total system Monte Carlo moves. The number of sticker–sticker interactions was calculated by counting the number of intermolecular interactions between aromatic beads (Phe or Tyr). Beads are interacting if they are within $\sqrt{3}$ lattice units. We performed five independent simulations, and the results shown aggregate all replicates.

Reporting summary

Further information on research design is available in the Nature Portfolio Reporting Summary linked to this article.

Data availability

Data necessary to interpret, verify and extend the research in this Article may be accessed via OSF at https://osf.io/3qm2c/ (ref. 77).

Code availability

Custom code utilized in this study, including RoSE and RoSEO3D, may be accessed via OSF at https://osf.io/3qm2c/ (ref. 76). RoSEO3D is under active development and publicly available on GitHub at https://github.com/Lew-Lab (ref. 77).

References

73. Wu, T., Lu, J. & Lew, M. D. Dipole-spread-function engineering for simultaneously measuring the 3D orientations and 3D positions of fluorescent molecules. *Optica* **9**, 505–511 (2022).
74. Mazidi, H., Lu, J., Nehorai, A. & Lew, M. D. Minimizing structural bias in single-molecule super-resolution microscopy. *Sci. Rep.* **8**, 13133 (2018).
75. Ferdman, B. et al. VIPR: vectorial implementation of phase retrieval for fast and accurate microscopic pixel-wise pupil estimation. *Opt. Express* **28**, 10179–10198 (2020).
76. Wu T. et al. Code and corpus of data for 'Single-fluorogen imaging reveals distinct environmental and structural features of biomolecular condensates'. *OSF* https://osf.io/3qm2c/ (2025).
77. Wu, T., Qiu, Y. & Lew, M. D. Active development of RoSEO3D, including updates. *GitHub* https://github.com/Lew-Lab (2025).

Acknowledgements

We thank J. Lu, N. A. Erkamp and M.-K. Shinn for help with the experiments. We thank T. Mittag and W. B. Borcherds for sharing their protocol for the expression and purification of the A1-LCD protein, and we thank L. E. Kay for sharing the *DDX4* gene. This work was funded by the Air Force Office of Scientific Research grant FA9550-20-1-0241 (to R.V.P.), the St. Jude Research Collaborative on the Biology and Biophysics of RNP granules (to R.V.P.) and the National Institutes of Health (grant F32GM146418 to M.R.K., grant R35GM124858 to M.D.L. and grant R01NS121114 to R.V.P.).

Author contributions

R.V.P. and M.D.L. conceived of and supervised the research. T.W., M.R.K. and Y.Q. designed and performed the imaging experiments and analysed the data with input from M.D.L. and R.V.P. M.R.K. prepared A1-LCD, Aro^+, Aro^- and DDX4 proteins, performed phase-separation assays and contributed intellectual insights. M.F. performed the LaSSI simulations and analysed the simulation results. T.W., M.R.K., M.D.L. and R.V.P. wrote and edited the manuscript with input from all authors.

Competing interests

The pixOL microscope used in this work was invented by T.W. and M.D.L. and is covered by US patent 11994470 B2 (2024), which was filed by and assigned to Washington University in St. Louis. R.V.P. is a member of the scientific advisory board of and a shareholder at Dewpoint Therapeutics Inc. The work reported here was not influenced by this affiliation. The remaining authors declare no competing interests.

Additional information

Extended data is available for this paper at https://doi.org/10.1038/s41567-025-02827-7.

Supplementary information The online version contains supplementary material available at https://doi.org/10.1038/s41567-025-02827-7.

Correspondence and requests for materials should be addressed to Rohit V. Pappu or Matthew D. Lew.

Peer review information *Nature Physics* thanks the anonymous reviewer(s) for their contribution to the peer review of this work.

https://doi.org/10.1038/s41567-025-02827-7

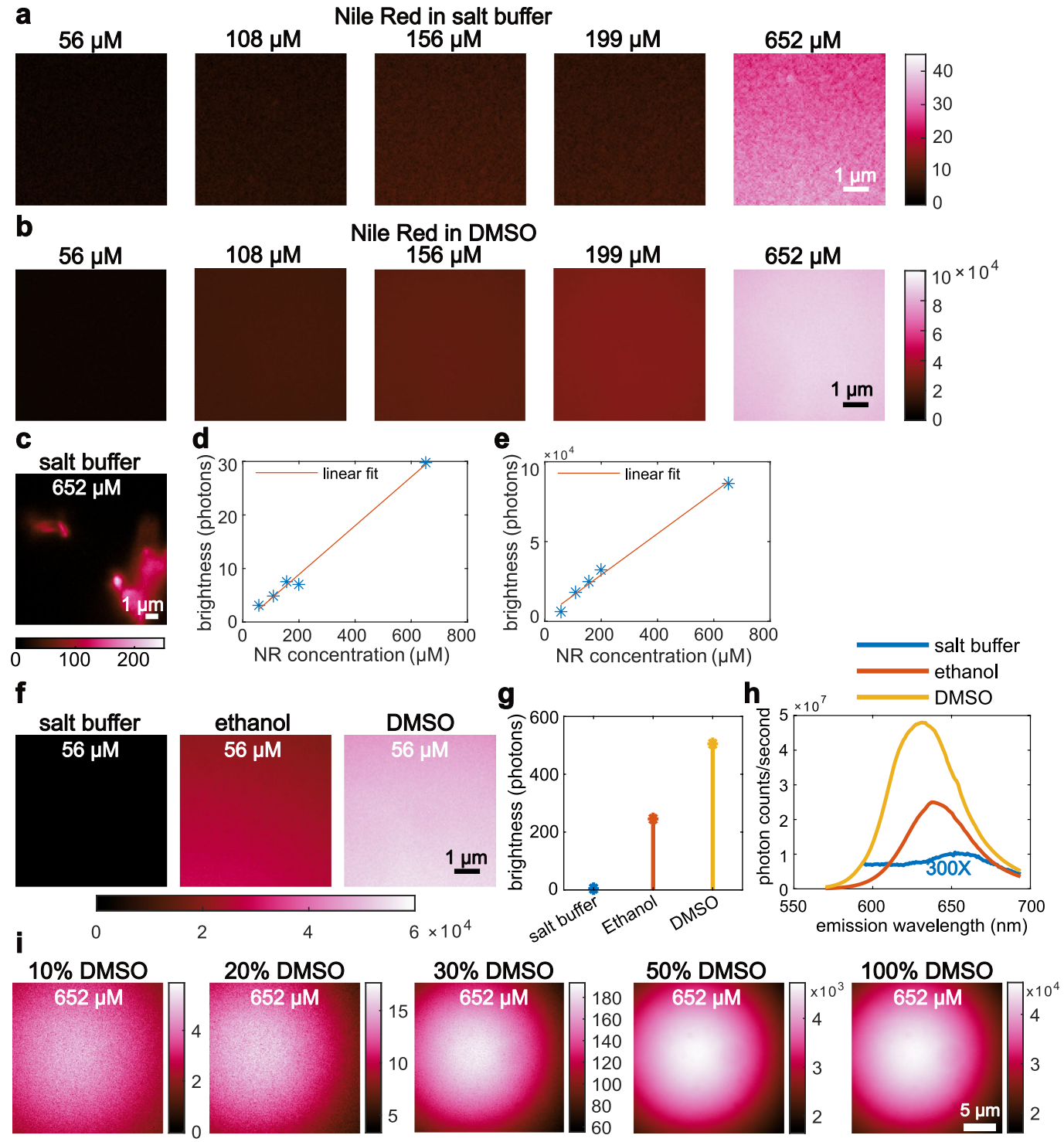

Extended Data Fig. 1 | See next page for caption.

https://doi.org/10.1038/s41567-025-02827-7

Extended Data Fig. 1 | Calibration of the Nile red (NR) dye in homogeneous solutions. a: The intensity of NR at different concentrations dissolved in an aqueous buffer comprising 20 mM HEPES with 300 mM NaCl. This buffer is identical to the one used for preparing A1-LCD condensates. Images were captured with the microscope focused on the coverslip. Note that the intensity increases with NR concentration. **b**: Intensity of NR at different concentrations dissolved in dimethyl sulfoxide (DMSO). Images were captured on the coverslip. The intensity increases with NR concentration. Comparing panels in **a** to panels in **b**, we see that at equivalent concentrations of NR, the intensities in DMSO are at least three orders of magnitude higher than in aqueous buffers. **c:** In aqueous buffers, molecules of NR form aggregates at or above concentrations of 652 μM. This image is captured above the coverslip. The morphologies of NR aggregates are different from the hubs we observed in condensates. **d**: and **e:** There is a linear correspondence between brightness, quantified in terms of the number of photons collected, and the concentration of fluorogens we use, both in aqueous buffers (d) and in DMSO (e). **f:** Fluorescence intensity of 56 μm NR solutions in different solvents. These measurements highlight the increased brightness of the solvatochromic NR as the hydrophobicity of the solvent increases. Calibration of the increase in fluorescence intensities is provided by the color bar. **g**: The data in (**f**) are summarized by plotting the average intensities of the images. **h**: The emission spectrum of NR in three different solvents. The emission spectrum of NR in the aqueous buffer is scaled by a factor of 300 for better visualization. The emission spectrum of NR is blue-shifted as the hydrophobicity of the solvent increases. **i:** The dielectric constant of 100% DMSO is 46.7 and that of aqueous solutions is ~78 at 296 K. At high concentrations of NR (652 μM), we quantified the fluorescence intensity as a function of % DMSO. These measurements show that the aggregates present in aqueous buffers (0% DMSO) are absent even in the presence of 10% DMSO. As the % of DMSO increases, the NR intensity increases by 2–4 orders of magnitude, thus highlighting the fluorogenic nature of NR. The experiments were conducted more than three times to ensure repeatability.

https://doi.org/10.1038/s41567-025-02827-7

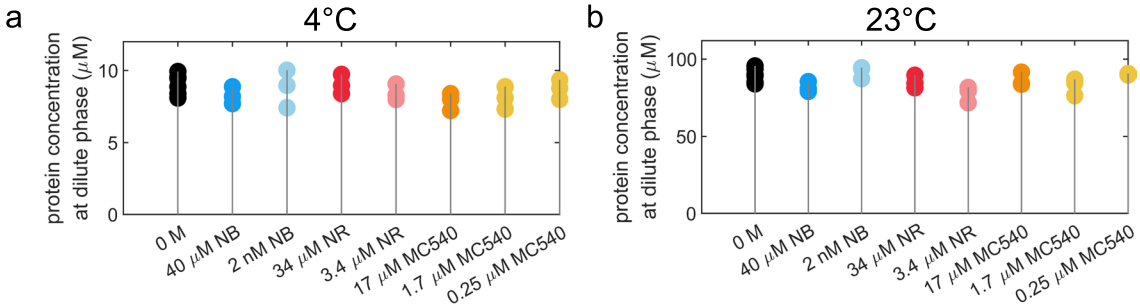

Extended Data Fig. 2 | Quantifying the effects of different fluorogens on the driving forces for phase separation. Driving forces were quantified by measuring saturation concentrations (c_{sat}) of A1-LCD molecules in the presence of different amounts of the different fluorogens used in this work. Within the error of the measurements, we find that adding Nile red (NR), Nile blue (NB), and merocyanine 540 (MC540) at different concentrations have minimal effects on the measured values of c_{sat}. This inference is made based on comparisons to measurements made in the absence of dyes (black circles). All measurements were performed using a starting concentration of 150 μM A1-LCD in 20 mM HEPES buffer and 300 mM NaCl at (**a**) 4 °C and (**b**) 23 °C. Prepared protein and dye mixtures were allowed to phase separate for 30 minutes at the indicated temperatures before the dilute phase was separated from the dense phase via centrifugation and protein concentration measured using absorbance at 280 nm. Each set of samples was prepared in triplicate and measured independently; each triplicate measurement is shown as individual filled circles.

https://doi.org/10.1038/s41567-025-02827-7

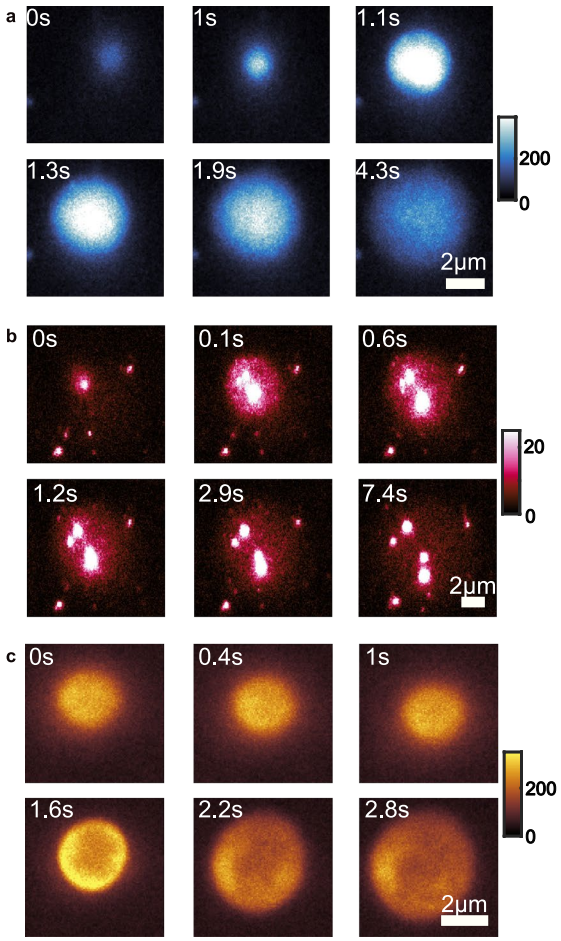

Extended Data Fig. 3 | Dynamic wetting of the glass coverslip by A1-LCD condensates. The images were captured using (**a**) NB, (**b**) NR, and (**c**) MC540. Colorbars: intensity (a.u.). The experiments were conducted more than three times to ensure repeatability.

https://doi.org/10.1038/s41567-025-02827-7

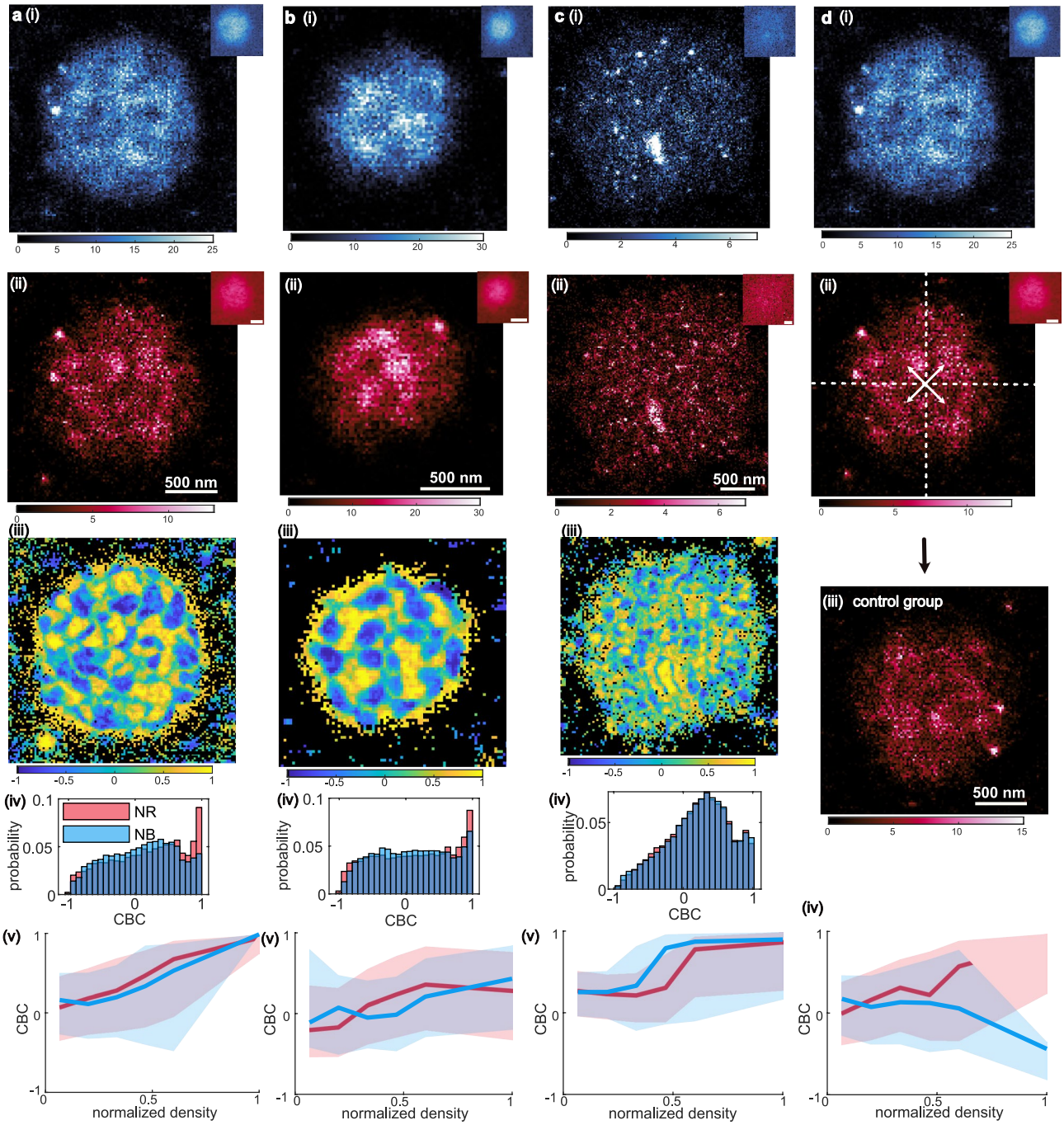

Extended Data Fig. 4 | Spatial inhomogeneities within A1-LCD condensates imaged by NB and NR are highly correlated. a, **b**, and **c**: Correlation between NB and NR measured for three different A1-LCD condensates. SMLM images of single condensates collected using (i) NB and (ii) NR. Insets: epifluorescence images. Color bars: number of single molecules within each 20 nm × 20 nm bin. (iii) Coordinate-based correlation (CBC) between NR and NB localizations averaged for localizations within each 20 nm × 20 nm bin. (iv) Distribution of CBC scores for (blue) NB and (red) NR. (v) CBC of NB (blue) and NR (red) plotted as a function of localization density. Solid lines: median value; shaded area: 25th-75th percentile. **d:** A condensate measured using (i) NB and (ii) NR as shown in **a**. We swapped emitters in the four regions of (ii) to form (iii) a modified NR condensate that should have weak correlations with the original condensate in **a**. (iv) CBC values between (i) NB localizations and (iii) the modified NR localizations.

https://doi.org/10.1038/s41567-025-02827-7

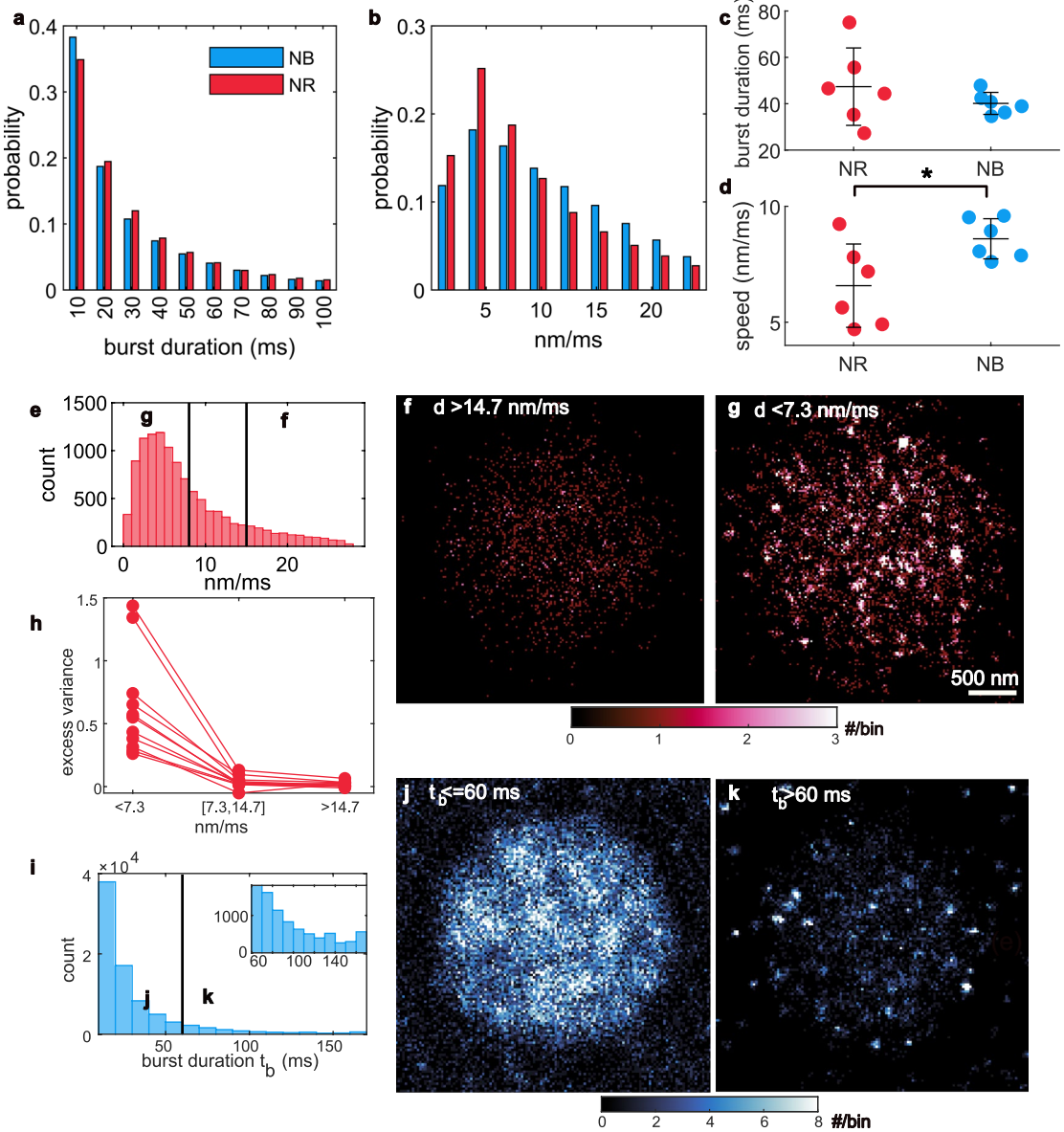

Extended Data Fig. 5 | Tracking single-molecule fluorescence bursts and speeds reveal inhomogeneous molecular distributions within A1-LCD condensates. a, b: Distribution of (**a**) burst durations and (**b**) speeds for NB (blue) and NR (red). **c**: Mean burst duration for individual condensates. **d**: Median speed for fluorogens within individual condensates ($p = 0.041$). * denotes p value < 0.05. All p values were calculated using Welch's unequal variances t-test (two-sided). Single-molecule tracking of (**e-h**) NR and (**i-k**) NB. **e:** NR speeds measured between consecutive camera frames (10 ms exposure time). **f, g:** SMLM images of NR with speeds (**f**) larger than 14.7 nm/ms and (**g**) shorter than 7.3 nm/ms. **h**: Excess variance of NR localizations grouped by speed (left: ≤ 7.3 nm/ms, middle: between 7.3/ms and 14.7 nm/ms, right: >14.7 nm/ms). Lines: excess variance of molecules within each condensate. **i:** Fluorescence burst durations t_b of NB. **j, k:** SMLM images of fluorogens (NB) with burst durations (**j**) shorter than 60 ms and (**k**) longer than 60 ms. Six condensates (18,300 ± 7,120 [mean ± SD] localizations each for NR, 49,300 ± 3,310 localizations each for NB) across two biological replicates were used to derive mean (center line) +/− SD (error bars).

https://doi.org/10.1038/s41567-025-02827-7

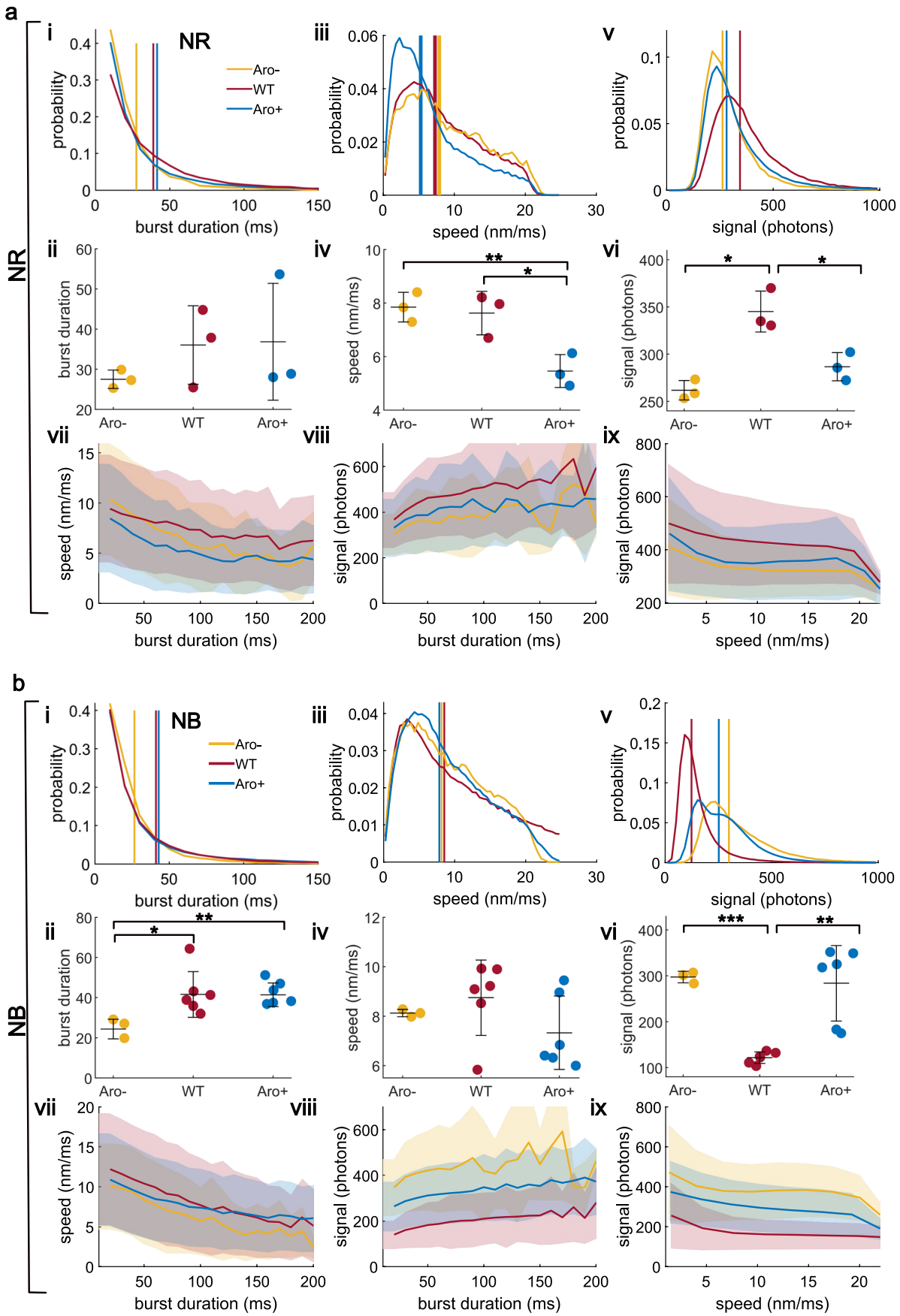

Extended Data Fig. 6 | See next page for caption.

https://doi.org/10.1038/s41567-025-02827-7

Extended Data Fig. 6 | Speeds and burst durations of NR and NB molecules within Aro$^-$, WT, and Aro$^+$ condensates. a, **b**: Measurements of (a) NR and (b) NB for three different LCDs. **i**, Distribution of burst duration. Vertical lines: mean burst durations. Yellow, Aro$^-$; red, WT; blue, Aro$^+$. **ii**, Mean burst duration for individual condensates. $p_{NB,Aro-,WT} = 0.016$, $p_{NB,Aro-,Aro+} = 0.0063$. **iii**, Distribution of speed. Vertical lines: median speeds. **iv**, Median speed for individual condensates. $p_{NR,Aro-,Aro+} = 0.0078$, $p_{NR,WT,Aro+} = 0.024$. **v**, Distribution of signal photons. Vertical lines: median signals. **vi**, Median signal of SMs in individual condensates. $p_{NR,Aro-,WT} = 0.011$, $p_{NR,WT,Aro+} = 0.023$, $p_{NB,Aro-,WT} = 3.0 \times 10^{-5}$, $p_{NB,WT,Aro+} = 0.004$. **vii**, Speeds of SMs as a function of their burst durations. **viii**, Signal photons of SMs as a function of their burst durations. **ix**, Signal photons as a function of their speed. Shaded region: ±1 standard deviation. For NR imaging, 3 Aro$^-$ (12,100 ± 3,140 [mean ± SD] localizations each), 3 WT (40,400 ± 12,300 localizations each), and 3 Aro$^+$ (49,300 ± 19,500 localizations each) condensates (technical replicates) were used to derive mean (center line) +/− SD (error bars). For NB imaging, 3 Aro$^-$ (30,300 ± 11,800 localizations each), 6 WT (60,400 ± 22,600 localizations each), and 6 Aro$^+$ (106,000 ± 53,200 localizations each) condensates across two biological replicates were used. * denotes p values < 0.05, ** denotes p values < 0.01, and *** denotes p values < 10^{-3}. All p values were calculated using Welch's unequal variances t-test (two-sided).

https://doi.org/10.1038/s41567-025-02827-7

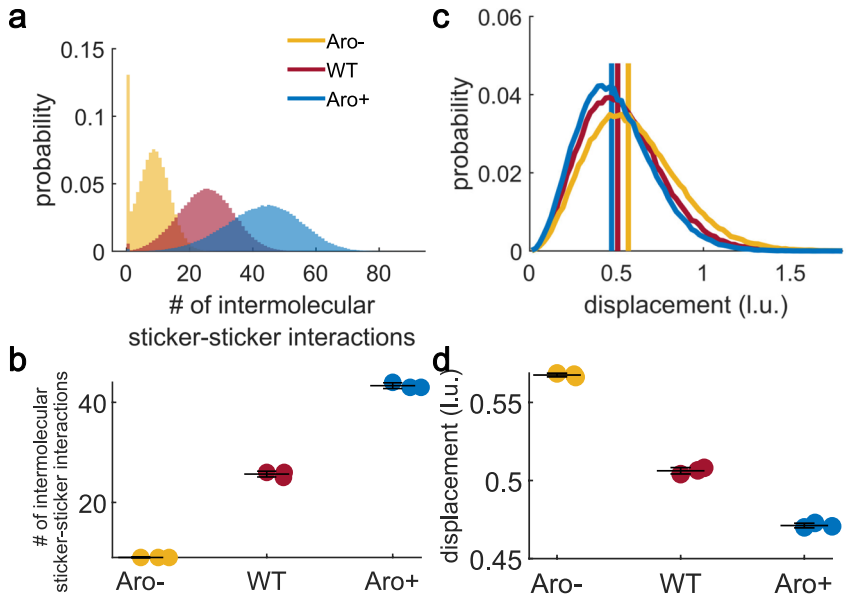

Extended Data Fig. 7 | LaSSI simulations of condensates formed by Aro$^-$, WT, and Aro$^+$. a: Distribution of the number of sticker-sticker interactions. Yellow, Aro$^-$; red, WT; blue, Aro$^+$. **b**: The median number of sticker-sticker interactions within individual condensates (reproduced from Fig. 4c). **c**: Distribution of displacement of protein chains. Vertical lines are the median displacements in lattice units (l.u). **d**: The median displacement of protein chains (reproduced from Fig. 4e). Mean (center line) ± 1 standard deviation (error bars) shown. Three independent simulations were performed for each of the three variants.

https://doi.org/10.1038/s41567-025-02827-7

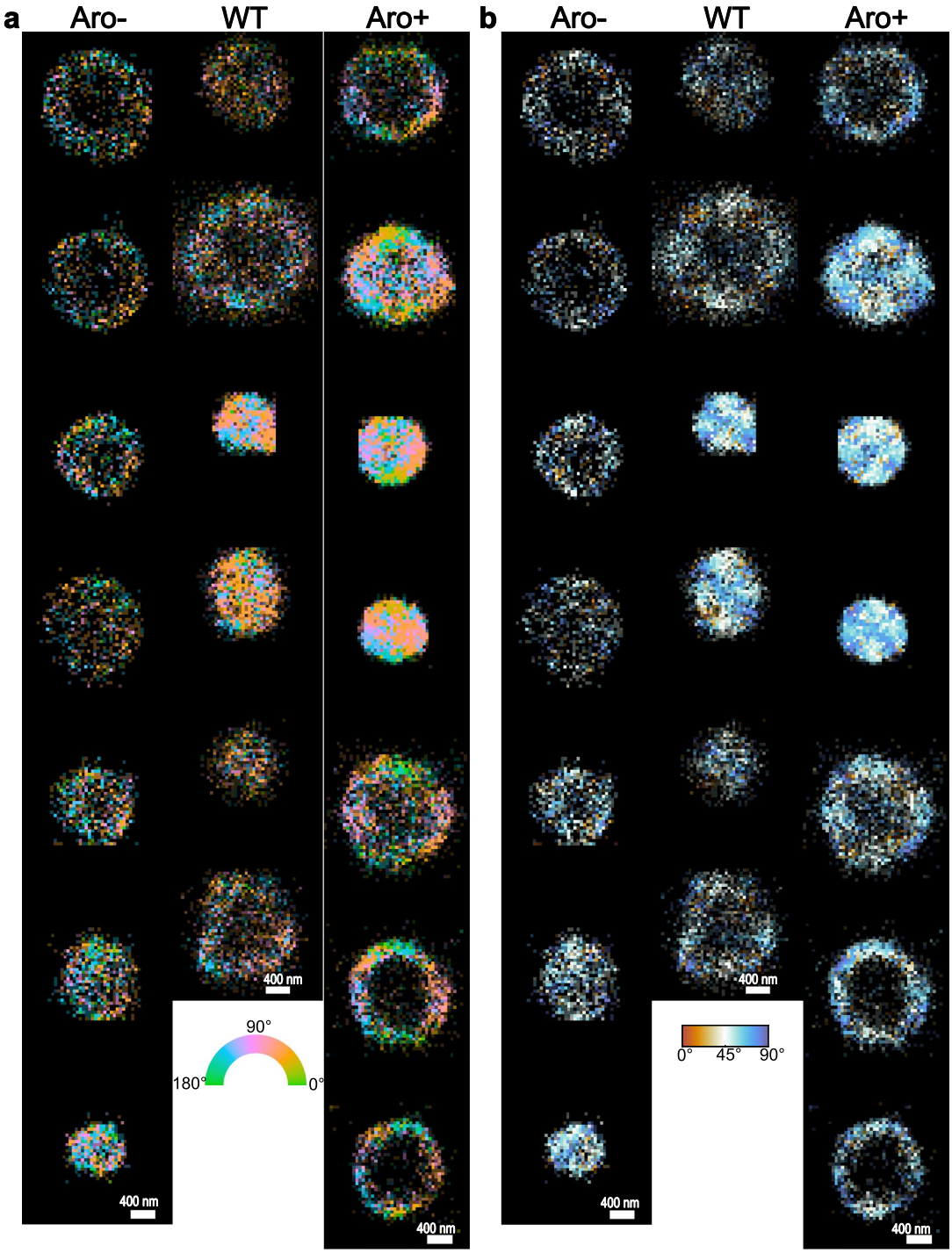

Extended Data Fig. 8 | Single-molecule orientation-localization microscopy (SMOLM) of Aro-, WT, Aro+ condensates. a: Single-molecule orientation image with colors representing the measured azimuthal angles φ in the xy-plane. **b:** Single-molecule orientation image with colors representing the orientation angle δ measured with respect to the normal vector to the condensate interface; the median angle δ is depicted within each 50 nm × 50 nm bin. The images are reconstructed from localizations of freely diffusing MC540.

https://doi.org/10.1038/s41567-025-02827-7

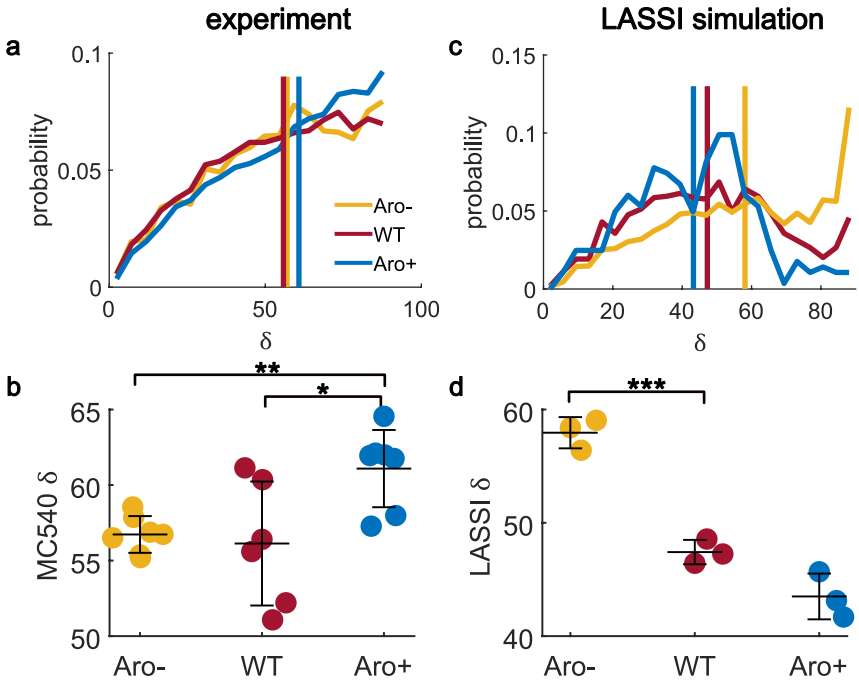

Extended Data Fig. 9 | Orientation of MC540 measured by SMOLM and orientation of protein chains quantified in LaSSI simulations of different condensates. a: Distribution of the orientation angle δ for MC540 measured with respect to the normal vector to the condensate interface using SMOLM. Vertical lines: median value of orientation δ. Yellow, Aro$^-$; red, WT; blue, Aro$^+$. **b**: Median δ values computed across individual condensates (circles, reproduced from Fig. 5e). Here, 7 Aro$^-$ (520 ± 75 [mean ± SD] localizations each), 6 WT (1,310 ± 703 localizations each), and 7 Aro$^+$ (2,170 ± 943 localizations each) condensates across three biological replicates were used to derive mean (center lines) +/− SD (error bars). $p_{Aro-,Aro+} = 0.0031$, $p_{WT,Aro+} = 0.033$. **c**: Distribution of orientation δ of protein chains in LaSSI simulations. Vertical lines: median orientation δ. **d:** δ values computed from LaSSI simulations using orientations of protein molecules at the interface (3 independent simulations per condensate type, reproduced from Fig. 5f). $p_{Aro-,WT} = 6.36 \times 10^{-4}$. * denotes p values < 0.05, ** denotes p values < 0.01, and *** denotes p values < 10^{-3}. All p values were calculated using Welch's unequal variances t-test (two-sided).

https://doi.org/10.1038/s41567-025-02827-7

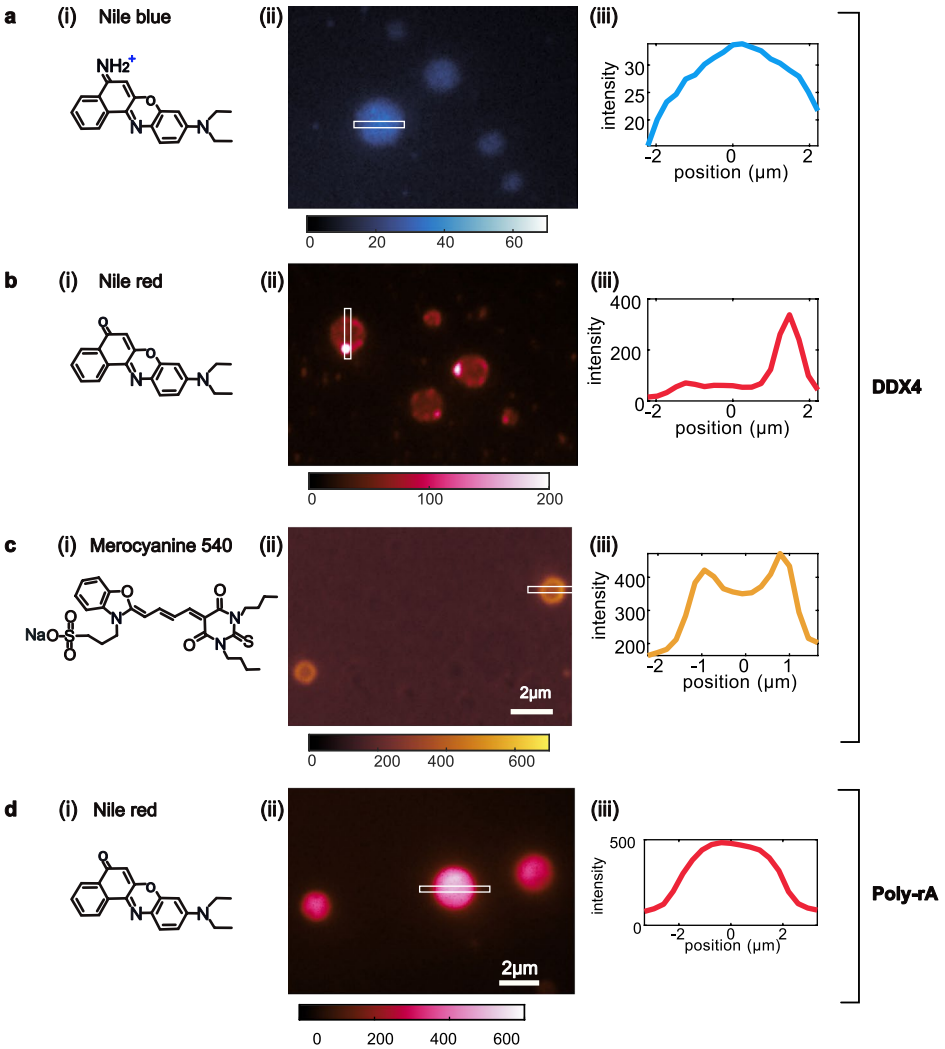

Extended Data Fig. 10 | Epifluorescence microscopy reveals that different fluorogenic probes sense chemical environments inside DDX4-IDR condensates from different perspectives. Imaging DDX4-IDR condensates using **a**. Nile blue (NB), **b**. Nile red (NR), and **c**. merocyanine 540 (MC540). (i) Chemical structures. (ii) Typical condensates as viewed by epifluorescence microscopy. (iii) Fluorescence intensity profiles along the long axis of white box shown in (ii). **d**. Imaging poly-rA condensates using NR. The experiments were conducted more than three times to ensure repeatability.

nature portfolio

Corresponding author(s): Rohit V. Pappu and Matthew D. Lew

Last updated by author(s): Jan 27, 2025

Reporting Summary

Nature Portfolio wishes to improve the reproducibility of the work that we publish. This form provides structure for consistency and transparency in reporting. For further information on Nature Portfolio policies, see our Editorial Policies and the Editorial Policy Checklist.

Statistics

For all statistical analyses, confirm that the following items are present in the figure legend, table legend, main text, or Methods section.

n/a	Confirmed	
☐	☒	The exact sample size (*n*) for each experimental group/condition, given as a discrete number and unit of measurement
☐	☒	A statement on whether measurements were taken from distinct samples or whether the same sample was measured repeatedly
☐	☒	The statistical test(s) used AND whether they are one- or two-sided *Only common tests should be described solely by name; describe more complex techniques in the Methods section.*
☒	☐	A description of all covariates tested
☒	☐	A description of any assumptions or corrections, such as tests of normality and adjustment for multiple comparisons
☐	☒	A full description of the statistical parameters including central tendency (e.g. means) or other basic estimates (e.g. regression coefficient) AND variation (e.g. standard deviation) or associated estimates of uncertainty (e.g. confidence intervals)
☐	☒	For null hypothesis testing, the test statistic (e.g. *F*, *t*, *r*) with confidence intervals, effect sizes, degrees of freedom and *P* value noted *Give P values as exact values whenever suitable.*
☒	☐	For Bayesian analysis, information on the choice of priors and Markov chain Monte Carlo settings
☒	☐	For hierarchical and complex designs, identification of the appropriate level for tests and full reporting of outcomes
☒	☐	Estimates of effect sizes (e.g. Cohen's *d*, Pearson's *r*), indicating how they were calculated

Our web collection on statistics for biologists contains articles on many of the points above.

Software and code

Policy information about availability of computer code

Data collection	Microscope images were collected using micro-manager version 2.0.3.
Data analysis	Custom code utilized in this study, including RoSE and RoSEO3D, may be accessed via OSF at https://osf.io/3qm2c/. RoSEO3D is under active development and are publicly available on GitHub at https://github.com/Lew-Lab. All other data analysis is performed using custom code, as described in the methods session and shared via OSF at https://osf.io/3qm2c/.

For manuscripts utilizing custom algorithms or software that are central to the research but not yet described in published literature, software must be made available to editors and reviewers. We strongly encourage code deposition in a community repository (e.g. GitHub). See the Nature Portfolio guidelines for submitting code & software for further information.

Data

Policy information about availability of data

All manuscripts must include a data availability statement. This statement should provide the following information, where applicable:

- Accession codes, unique identifiers, or web links for publicly available datasets
- A description of any restrictions on data availability
- For clinical datasets or third party data, please ensure that the statement adheres to our policy

Data necessary to interpret, verify, and extend the research in this article may be accessed via OSF at https://osf.io/3qm2c/. Additional data are available upon reasonable request to the corresponding authors.

Research involving human participants, their data, or biological material

Policy information about studies with human participants or human data. See also policy information about sex, gender (identity/presentation), and sexual orientation and race, ethnicity and racism.

Reporting on sex and gender	This research does not involve human participants.
Reporting on race, ethnicity, or other socially relevant groupings	This research does not involve human participants.
Population characteristics	This research does not involve human participants.
Recruitment	This research does not involve human participants.
Ethics oversight	This research does not involve human participants.

Note that full information on the approval of the study protocol must also be provided in the manuscript.

Field-specific reporting

Please select the one below that is the best fit for your research. If you are not sure, read the appropriate sections before making your selection.

☒ Life sciences ☐ Behavioural & social sciences ☐ Ecological, evolutionary & environmental sciences

For a reference copy of the document with all sections, see nature.com/documents/nr-reporting-summary-flat.pdf

Life sciences study design

All studies must disclose on these points even when the disclosure is negative.

Sample size	No statistical method was used to predetermine sample size. At least 3 condensates per field of view (FOV) and 3 FOVs per independent experiment were observed/measured for consistency. Single-molecule statistics utilize 500-10^5 localizations per condensate, depending on the experiment, which enables reliable calculations of means, medians, and standard deviations as necessary.
Data exclusions	No data were excluded from the analyses, except when filtering or thresholds were applied during image analysis as detailed in the Methods section.
Replication	All experiments were repeated a minimum of 3 times using independent preparations. Biological replicates are defined as condensates that are prepared either from batches of protein that have been purified from distinct bacterial expressions or condensates that have been prepared from a stock of protein that is kept in long-term storage for up to six months.
Randomization	Data collection and experimental conditions were not randomized.
Blinding	Data collection and analysis were not performed blind to the conditions of the experiments.

Reporting for specific materials, systems and methods

We require information from authors about some types of materials, experimental systems and methods used in many studies. Here, indicate whether each material, system or method listed is relevant to your study. If you are not sure if a list item applies to your research, read the appropriate section before selecting a response.

Materials & experimental systems

n/a	Involved in the study
☒	☐ Antibodies
☒	☐ Eukaryotic cell lines
☒	☐ Palaeontology and archaeology
☒	☐ Animals and other organisms
☒	☐ Clinical data
☒	☐ Dual use research of concern
☒	☐ Plants

Methods

n/a	Involved in the study
☒	☐ ChIP-seq
☒	☐ Flow cytometry
☒	☐ MRI-based neuroimaging

Plants

Seed stocks	n/a
Novel plant genotypes	n/a
Authentication	n/a